Soil Dynamics and Earthquake Engineering 92 (2017) 503–527

Contents lists available at ScienceDirect

Soil Dynamics and Earthquake Engineering

journal homepage: www.elsevier.com/locate/soildyn

Seismic wave amplification by topographic features: A parametric study

Babak Poursartip[a], Arash Fathi[b], Loukas F. Kallivokas[a,b,*]

[a] Department of Civil, Architectural, and Environmental Engineering, The University of Texas at Austin, Austin, TX, USA
[b] The Institute for Computational Engineering & Sciences, The University of Texas at Austin, Austin, TX, USA

ARTICLE INFO

Keywords:
Topography effects
Seismic amplification
Site response
Seismic wave propagation

ABSTRACT

Despite the ever increasing adoption of wave motion simulations for assessing seismic hazard, most assessment/simulations are still based on a flat surface earth model. The purpose of this paper is to quantify the effect of topographic irregularities on the ground motion and local site response by means of parametric investigations in the frequency-domain of typical two-dimensional features.

To this end, we deploy best-practice tools for simulating seismic events in arbitrarily heterogeneous formations; these include: a forward wave simulator based on a hybrid formulation encompassing perfectly-matched-layers (PMLs); unstructured spectral elements for spatial discretization; and the Domain-Reduction-Method that permits placement of the seismic source within the computational domain, thus allowing consideration of realistic seismic scenarios.

Of particular interest to this development is the study of the effects that various idealized topographic features have on the surface motion when compared against the response that is based on a flat-surface assumption. We report the results of parametric studies for various parameters, which show motion amplification that depends, as expected, on the relation between the topographic feature's characteristics and the dominant wavelength. More interestingly, we also report motion de-amplification patterns.

1. Introduction

Understanding and quantifying the seismic response in regions with surface irregularities, such as hills, valleys, and alluvial basins, have been the focus of seismologists and earthquake engineers for decades. The interest remains strong since discrepancies still exist between the recorded surface motion from strong earthquakes and numerical simulations. There are many reasons for the discrepancies, but chief among them are uncertainties about the subsurface properties (velocity model, fault location/geometry, etc.) used in seismic motion simulations, uncertainties in quantifying the seismic source mechanisms, and the lack of adequate representation of topographic features. Empirical evidence following strong earthquakes suggests that topographic features may induce amplification, and even de-amplification, in the proximity of a topographic feature. For example, Fig. 1 depicts damage following the 2010 Haiti earthquake, where buildings closer to the hill's crest suffered more damage than those along the hill's side.

The literature on the effect of surface geometry on wave motion falls into three general categories: (i) observations from earthquakes and field experiments; (ii) studies based on analytical and semi-analytical solutions for simple topographic geometries, such as a triangular wedge or a semi-circular valley; and (iii) parametric studies based on numerical simulations. In the first category, examples include observations in the aftermath of the 1971 San Fernando Valley earthquake [13]; the 1987 Whittier Narrows earthquake [27]; and the 2002 Molise earthquake in Italy [32]. Çelebi [15] investigated the topological amplification of the 1985 Chile earthquake and reported on the damage pattern to structures situated on ridges and soft soil sites. He concluded that the unusual patterns of structural damage resulted from frequency-dependent amplification due to the surface irregularities. Later, in 1991 [16], Çelebi collected and summarized the results of case studies on three earthquakes, and provided evidence of topographic amplification for a particular range of frequencies. Hartzell et al. [23] studied the cause of the structural damage and ground cracking observed at the Robinwood Ridge during the 1989 Loma Prieta earthquake and argued that the presence of ridges intensifies the motion amplification.

Assimaki studied the 1999 Athens earthquake in Greece [5,7] and showed that the observed amplification of seismic motion in the vicinity of a cliff crest could only be predicted by simultaneously accounting for the topographic geometry, stratigraphy, and nonlinearity. The analysis of the Tarzana Hill recordings from the 1987 Whittier Narrows and the 1994 Northridge earthquakes by Graizer [22] showed that the observed amplification was due to the combined effects of

* Corresponding author at: The Institute for Computational Engineering & Sciences, The University of Texas at Austin, Austin, TX, USA.
E-mail addresses: babakp@utexas.edu (B. Poursartip), arash.fathi@utexas.edu (A. Fathi), loukas@mail.utexas.edu (L.F. Kallivokas).

http://dx.doi.org/10.1016/j.soildyn.2016.10.031
Received 20 July 2016; Received in revised form 21 October 2016; Accepted 24 October 2016
Available online 09 November 2016
0267-7261/

Fig. 1. Destruction pattern on the hill crest following the 2010 Haiti earthquake.

topography and layering that resulted in trapping energy within a low-velocity layer near the surface. Similar observations were also reported in [42,43,52,53]. Further reviews on observations on seismic amplification can be found in Massa et al. [33], and Buech et al. [14].

Field experiments could also provide insight into the effect topography plays in seismic amplification, but due to cost considerations there have only been a few reported attempts. Buech et al. [14] installed a seismic array along the crest of a hill in New Zealand to record earthquake data. They reported large amplification along the crest, as large as eleven times of the motion on the flat surface. Massa et al. [33] performed a similar experiment using data from a seismic network installed on a ridge in central Italy. They reported amplification as large as 4.5 at specific frequencies. More recently, Wood and Cox [58] exploited ground shaking generated in a coal mine in central Utah and reported significant amplitude changes due to topography. Similar field experiments can also be found in [23,38,40].

Whereas exact solutions of wave motion in a homogeneous, flat-surface, half-space are readily available, closed-form solutions for a half-space exhibiting a surface irregularity, even one described by a canonical shape, are scantier. Among such exact solutions, the greatest attention has been paid to the scattering of SH waves, owing to the scalar form of the associated wave equation. One of the earliest studies is due to Sills [51] where a method was developed to solve the scattering of SH waves by an arbitrary topography in a homogeneous, semi-infinite half-space using an integral equation. Sills applied the method to a semi-circular hill, to a Gaussian hill, and to a combination of a hill and a valley for various wave motion characteristics. Trifunac [55] presented a closed-form solution for the diffraction of SH waves by a semi-cylindrical canyon and reported strong amplification near the feature. Sánchez-Sesma et al. [47] developed a boundary integral method for the scattering of SH waves by any irregular feature. In 1985, Sánchez-Sesma [49] described another method particularly suited for infinite wedge-shaped hills and valleys.

Exact solutions for the vector equation, accounting for P and SV waves in the presence of a surface feature are rare. One exception is the analytical solution proposed by Sánchez-Sesma for an infinite wedge [50]. Paolucci [39] has also provided a simple approximate expression for the fundamental frequency of triangular hills.

In the absence of exact solutions, numerical tools have long been used for simulating wave motion in complex domains. We cite representative works, classified according to the underlying numerical method: (i) finite difference method-based approaches (FDM), which are simple to apply but have difficulties with modeling of the complex surfaces [13,36,37,54], (ii) boundary element-based methods (BEM), which have the advantage of dimensionality reduction, but are limited to cases for which the Green's functions are available. Two major BEM approaches exist, direct (DBEM) and indirect (IBEM). Examples of (DBEM) include the works by Wong and Jennings [57], Álvarez-Rubio et al. [1], Kamalian et al. [24] and, Nguyen and Gatmiri [35], whereas examples of IBEM include the works by Sánchez-Sesma and Campillo [46], Sánchez-Sesma et al. [48], Luzón et al. [31], Gil-Zepeda et al. [20], and Rodríguez-Castellanos et al. [44]. (iii) finite element-based approaches (FEM) which include the works of Moczo et al. [34], Assimaki et al. [6,8], Chaljub et al. [17], Peter et al. [41], and Kucukcoban and Kallivokas [30]. (iv) spectral element-based methods (SEM), that have all the advantages of finite elements, while also allow for easy parallelization. See, for example, Komatitsch and Tromp [28], Komatitsch and Vilotte [29], and Fathi et al. [19].

A few parametric studies conducted so far shed light on the problem of seismic amplification. Ashford and Sitar [2], and Ashford et al. [3] performed a frequency domain parametric study on the effect of single-slope topography on the propagation of shear waves. Assimaki et al. [4,5] affirmed the significance of topography by performing a time-domain parametric study on a single slope geometry. They concluded that the frequency content of the excitation, stratigraphy, and the geometry of the cliff are all important in the amplification of incoming seismic waves.

Although much work has been done to date, the influence of surface topography is still neglected in seismic code provisions, since the codification of the links between amplification and topographic characteristics remains a challenge.

The main goal of this paper is to contribute to a better understanding of the effects of surface topography on site response by means of a systematic parametric investigation. To this end, we consider parameters such as feature geometry, incident wave type, angle of incidence, Poisson's ratio, and incident wave frequency. In this study, we focus on P and SV waves, and omit SH waves because their effects have already been addressed in the literature. In the following, we first describe the key components of a software toolchain developed for conducting the parametric study. Numerical examples validating the methodology against known solutions appear in Appendix B. The results of the parametric studies involving idealized hills and valleys follow the methodology presentation.

2. Wave motion simulation methodology

We briefly discuss an approach that deploys best-practice tools for simulating seismic events in arbitrarily heterogeneous formations. The approach includes: a forward explicit wave solver based on a hybrid formulation that includes perfectly-matched-layers (PMLs) for limiting the computational domain; the Domain-Reduction-Method that permits placement of seismic sources within the computational domain; unstructured spectral elements for spatial discretization; and parallelizing tools that allow for a scalable and cost-effective numerical simulation of wave propagation.

The use of a domain discretization method (finite or spectral elements) requires that the extent of the semi-infinite physical domain be truncated to form a finite computational domain by introducing appropriate absorbing boundary conditions at the truncation surfaces. To this end, we make use of an unsplit-field Perfectly-Matched-Layer formulation, described in Kucukcoban and Kallivokas [30], and in Fathi et al. [19].

Accordingly, the original semi-infinite physical domain is reduced to a finite domain (Fig. 2), which is further partitioned into the interior computational domain Ω, and the surrounding PML buffer zone. Per [19,30], the formulation leads to the following equations of motion for the discrete problem (in the frequency domain):

$$(-\omega^2\mathbf{M} + i\omega\mathbf{C} + \mathbf{K})\mathbf{d} = \mathbf{f}, \tag{1}$$

where the various matrices and vectors are defined as:

$$\mathbf{M} = \begin{bmatrix} \overline{\mathbf{M}}_{\mathrm{RD}} + \overline{\mathbf{M}}_a & \mathbf{0} \\ \mathbf{0} & \mathbf{N}_a \end{bmatrix}, \mathbf{C} = \begin{bmatrix} \overline{\mathbf{M}}_b & \overline{\mathbf{A}}_{eu} \\ -\overline{\mathbf{A}}_{el}^T & \mathbf{N}_b \end{bmatrix}, \mathbf{K} = \begin{bmatrix} \overline{\mathbf{K}}_{\mathrm{RD}} + \overline{\mathbf{M}}_c & \overline{\mathbf{A}}_{pu} \\ -\overline{\mathbf{A}}_{pl}^T & \mathbf{N}_c \end{bmatrix},$$
$$\mathbf{d} = [\mathbf{U} \quad \Sigma]^T, \quad \mathbf{f} = [\bar{\mathbf{f}}_{\mathrm{RD}} \quad \mathbf{0}]^T. \tag{2}$$

In (1), the subscript RD denotes the regular/physical domain, and

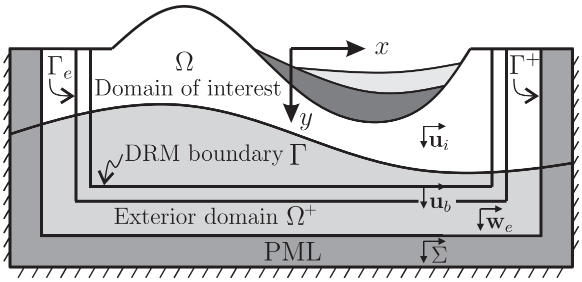

Fig. 2. Computational domain partitioned in interior domain Ω; exterior domain Ω^+; DRM boundary; and PML buffer.

$\mathbf{M}_{\mathrm{RD}}$, $\mathbf{K}_{\mathrm{RD}}$, and $\mathbf{f}_{\mathrm{RD}}$ are standard mass matrix, stiffness matrix, and vector of nodal forces, respectively. $\mathbf{d}$ and $\mathbf{f}$ are the displacement/stress and force vectors, respectively. A bar on a submatrix indicates its extension to encompass all the displacement degrees-of-freedom. The rest of the submatrices in (2) correspond to the PML buffer zone, and are explained in detail in [19,30]. $\mathbf{d}$, the unknown vector, consists of the nodal displacements $\mathbf{U}$, partitioned such that the regular domain displacements are first, followed by the displacements on the interface boundary between the interior domain and the PML buffer, and finally the displacements in the PML buffer zone; Σ are the unknown stress components in the PML.

Eq. (1) does not readily account for a seismic event. Our primary interest in this study is to be able to accommodate incoming plane waves at various angles of incidence and frequencies, thus simulating an earthquake originating from deep in the earth. To this end, we turn to the Domain-Reduction-Method (DRM) developed by Bielak et al. [11,12,18,59]. The DRM proposes a two-step approach for incorporating the effects of the seismic source. In a first step, the free-field solution is obtained for a traveling plane wave by subtracting the local heterogeneities or geometric irregularities of the region of interest. In a second step, the heterogeneities and/or topographic features are re-introduced and the equations of motion are appropriately modified to account for the incoming motion. The latter is accomplished by the introduction of the DRM boundary —a one-element wide layer— separating the domain of interest containing the topographic feature from the exterior domain, where the latter is the region between the DRM and the PML (Fig. 2). Per the DRM formulation, the unknowns comprise the total motion within the interior domain of interest and the scattered motion within the exterior domain. It is on the DRM boundary that the incoming motion is prescribed. Accordingly, the equations of motion (1) are modified to read:

$$(-\omega^2\widetilde{\mathbf{M}} + i\omega\widetilde{\mathbf{C}} + \widetilde{\mathbf{K}})\widetilde{\mathbf{d}} = \tilde{\mathbf{f}}, \tag{3}$$

where:

$$\widetilde{\mathbf{M}} = \begin{bmatrix} \mathbf{M}_{ii}^{\Omega} & \mathbf{M}_{ib}^{\Omega} & \mathbf{0} & \mathbf{0} \\ \mathbf{M}_{bi}^{\Omega} & \mathbf{M}_{bb}^{\Omega} + \mathbf{M}_{bb}^{\Omega^+} & \overline{\mathbf{M}}_{be}^{\Omega^+} & \mathbf{0} \\ \mathbf{0} & \overline{\mathbf{M}}_{eb}^{\Omega^+} & \overline{\mathbf{M}}_{ee}^{\Omega^+} + \overline{\mathbf{M}}_a & \mathbf{0} \\ \mathbf{0} & \mathbf{0} & \mathbf{0} & \mathbf{N}_a \end{bmatrix}, \widetilde{\mathbf{C}} = \begin{bmatrix} \mathbf{0} & \mathbf{0} & \mathbf{0} & \mathbf{0} \\ \mathbf{0} & \mathbf{0} & \mathbf{0} & \mathbf{0} \\ \mathbf{0} & \mathbf{0} & \overline{\mathbf{M}}_b & \overline{\mathbf{A}}_{eu} \\ \mathbf{0} & \mathbf{0} & -\overline{\mathbf{A}}_{el}^T & \mathbf{N}_b \end{bmatrix},$$

$$\widetilde{\mathbf{K}} = \begin{bmatrix} \mathbf{K}_{ii}^{\Omega} & \mathbf{K}_{ib}^{\Omega} & \mathbf{0} & \mathbf{0} \\ \mathbf{K}_{bi}^{\Omega} & \mathbf{K}_{bb}^{\Omega} + \mathbf{K}_{bb}^{\Omega^+} & \overline{\mathbf{K}}_{be}^{\Omega^+} & \mathbf{0} \\ \mathbf{0} & \overline{\mathbf{K}}_{eb}^{\Omega^+} & \overline{\mathbf{K}}_{ee}^{\Omega^+} + \overline{\mathbf{M}}_C & \overline{\mathbf{A}}_{pu} \\ \mathbf{0} & \mathbf{0} & -\overline{\mathbf{A}}_{pl}^T & \mathbf{N}_C \end{bmatrix}, \tilde{\mathbf{f}} = \begin{bmatrix} \mathbf{0} \\ -\mathbf{M}_{be}^{\Omega^+}\ddot{\mathbf{u}}_e^0 - \mathbf{K}_{be}^{\Omega^+}\mathbf{u}_e^0 \\ \mathbf{M}_{eb}^{\Omega^+}\ddot{\mathbf{u}}_b^0 + \mathbf{K}_{eb}^{\Omega^+}\mathbf{u}_b^0 \\ \mathbf{0} \end{bmatrix},$$

$$\widetilde{\mathbf{d}} = [\mathbf{u}_i \;\; \mathbf{u}_b \;\; \mathbf{w}_e \;\; \boldsymbol{\Sigma}]^T. \tag{4}$$

The subscripts i, e, and b refer to nodes in the interior domain of interest Ω, the exterior domain Ω^+, and the DRM boundary Γ, respectively. $\mathbf{u}_i$ and $\mathbf{u}_b$ denote total motion displacement vectors, whereas $\mathbf{w}_e$ denotes the scattered motion displacement vector.

The approach has been implemented in a parallel code, with the aid of PETSc [9], where the Metis [26] mesh partitioner has been used.

3. Description of study parameters

We consider a homogeneous medium with mass density $\rho = 2000\ \mathrm{kg/m^3}$, shear modulus $G = 100\ \mathrm{MPa}$, and Poisson's ratio $\nu = 0.25$. The majority of the simulations are based on this material model. Additionally, to study the effect of Poisson's ratio on the wave motion, two extra material models are considered with Poisson's ratios $\nu = 0.33$ and $\nu = 0.40$, and otherwise identical mass density and shear modulus. The simulations are performed in the frequency domain without any material damping.

We consider only symmetric hills and valleys to describe surface irregularities. The schematic configuration of the corresponding computational domains are plotted in Fig. 3, where b denotes the base of the feature, and h is the height or depth of the hill or valley, respectively. We introduce the shape ratio $S_r = \arctan(h/b)$ to quantify the slenderness of each shape. We also introduce the dimensionless frequency:

$$\eta = \frac{h}{\lambda_s}, \tag{5}$$

which is the ratio of the feature's height or depth to the shear wavelength, in order to normalize the incident wave frequency.

We truncate the semi-infinite physical domain such that the distance from the feature to the truncation boundary is at least three times the shear wavelength λ_s. The computational domain has been surrounded on its sides and bottom by a ten-element-thick PML. We discretize the computational domain using quadratic quadrilateral elements with element size that allows for at least 40 points per shear wavelength.

In summary, we perform the parametric study using the following

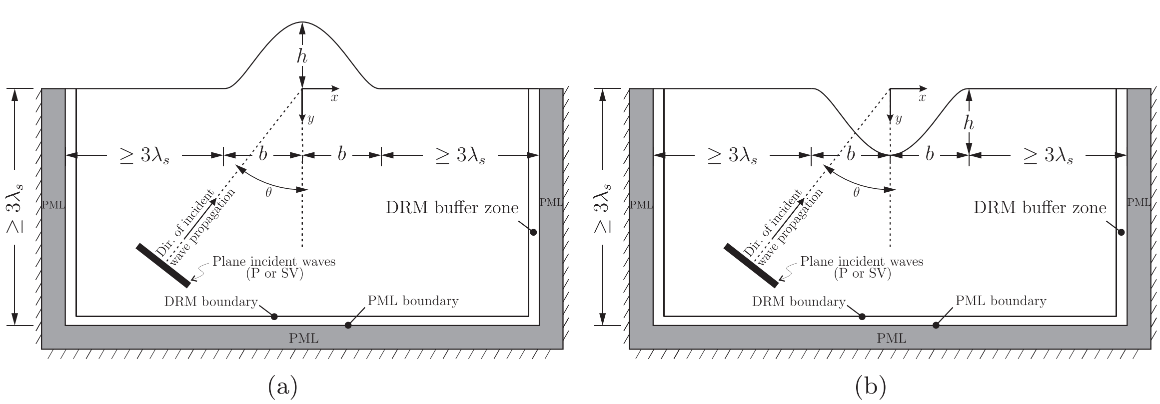

Fig. 3. Typical geometry of topographic features used in this study: (a) hills, and (b) valleys.

parameters:

- wave types: plane P- and SV-waves.
- angle of incidence: 0–45° for P incidence, and 0–35° for SV incidence in 5° increments.
- incident wave frequency: η varies from 0.1 to 5.0, in 0.1 increments.
- topography: hills and valleys of different geometry.
- topography shape ratio: the inverse tangent of height to base ratio, $\arctan(h/b)$.

4. Parametric study on hills

In this section, we report on the effects of the hill's geometry, the wave type, wave frequency, angle of incidence, and Poisson's ratio on the motion amplification/de-amplification.

4.1. Effects of feature's geometry

To investigate the influence of a feature's shape on the resulting motion, we consider: (i) the effect of the geometry idealization, i.e., how differences in similar shapes may affect amplification, and (ii) the effect of shape ratio (the height to base ratio) for a fixed geometry. We report first on the feature's shape effects.

Four different hill geometries have been previously reported in the literature: (i) Semi-elliptical and semi-circular hills used in [46,51,56]; (ii) Bell-shaped hills with an exponential function (bell-e) proposed in [10,51,60]; (iii) Bell-shaped hills described by a cosine function (bell-c) [25]; and (iv) triangular hills [45,46,50]. We perform the parametric study on all four shapes to review the effects of topography idealization on wave amplifications. The geometry and the area of these hills are described in Table 1 using a coordinate system whose origin is on the surface. Fig. 4 depicts all four shapes for a common height $h = 100$ m and a base $b = 100$ m. Note that the semi-circular geometry has the largest area, and the bell-e hill is the steepest idealized hill with the smallest area. The triangular and bell-c hills have equal areas and, indeed, the bell-c hill is a smoothened version of the triangular shape without the sharp corners. In all cases, the half-space is homogeneous with a Poisson's ratio $\nu = 0.25$.

A sharp corner in the path of the plane waves on the surface would generate Rayleigh waves, whose amplitudes depend highly on the geometry of the hill and the sharpness of the corner. The maximum surface displacement in many cases occurs when the generated Rayleigh waves interfere constructively with each other within the feature. This is a key reason that different hill geometries show different amplifications.

Fig. 5 compares the maximum displacements on the surface of the four idealized hills due to vertically propagating plane waves with frequencies ranging from $\eta = 0.1$ to 2.0, in increments of 0.1. The maximum displacement in this figure is normalized with respect to the flat surface solution u^{ff}, whenever the latter is non-zero (Appendix A).

We note first the fluctuating amplification pattern of the semi-circular hill; for the other three shapes, the variation of amplification follows a smoother trend. For example, the horizontal amplification of

Table 1
The geometry of hills for $(-b \le x \le b)$, Out of this range $y(x) = 0.0$.

Feature's name	Geometry	Cross section area
Semi-elliptical	$y(x) = h\sqrt{1 - (\frac{\lvert x\rvert}{b})^2}$	$\frac{\pi}{2}bh$
Bell-c	$y(x) = 0.5h(1 + \cos(\pi\frac{\lvert x\rvert}{b}))$	bh
Bell-e	$y(x) = h(1 - (\frac{\lvert x\rvert}{b})^2)\exp(-3(\frac{\lvert x\rvert}{b})^2)$	$0.86bh$
Triangle	$y(x) = h(1 - \frac{\lvert x\rvert}{b})$	bh

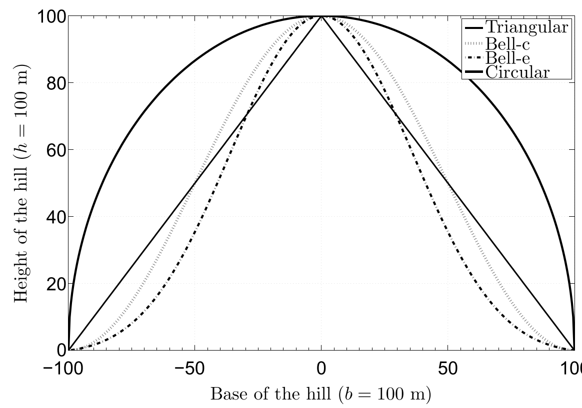

Fig. 4. Geometry of four idealized hills for a common height of $h = 100$ m and base $b = 100$ m.

the semi-circular hill is 2.70 for an incident P-wave of frequency $\eta = 0.5$, while the amplification for the other geometries is around 1.20; by contrast, for $\eta = 1.5$ the semi-circular amplification is 1.52, while it is 2.55 for the triangular hill. We conjecture that at certain frequencies, the convexity of the semi-circular feature assists in the trapping of energy better than any other of the three shapes.

The other distinct pattern is the difference between the amplifications of the triangular and bell-c hills, even though they have equal areas. For instance, the vertical displacement due to an incident SV with frequency $\eta = 1.5$ is only 2.01 for the triangular hill, however, it is 3.40 for the bell-c hill. The difference can be attributed to the sharper corners that the triangular hill has in comparison to the bell-c hill that leads to strong Rayleigh wave patterns within the feature. We also note that the two smooth bell-shaped hills, though very close in shape, experience different amplifications, particularly for the horizontal component due to P incidence (Fig. 5(c)). For example, the bell-c hill horizontal amplification is 2.25 for $\eta = 0.8$, while it is 1.76 for the bell-e hill. In summary, the observed differences between the amplifications indicate the strong effect the feature's idealization has on the amplification patterns.

Fig. 6 depicts the maximum surface amplifications of different geometries for plane waves with angle of incidence $\theta = 15°$. Similar conclusions can be made for this angle of incidence, even though the amplifications are overall larger in comparison to the vertical incidence. The amplification pattern of the semi-circular hill is more rugged as opposed to the smoother amplification patterns of the other geometries. For example, the horizontal amplification of the semi-circular hill is 4.40 for an incident P with frequency $\eta = 0.5$, while the amplification for the other geometries is around 2.70; the vertical amplification varies from 3.6 for the semi-circular hill to 5.35 for the bell-c hill, 4.7 for triangular and 6.35 for the bell-e for an incident SV with frequency $\eta = 1.0$, i.e., with a wavelength equal to the feature's height or, equal to half of the feature's base. There are again differences between the two bell-shaped hills: for example, the vertical amplification due to SV incidence is 5.3 for the bell-c shape at $\eta = 1.0$, but the corresponding bell-e shape amplification is 6.2. For most frequencies, the bell-c hill yields larger amplifications for SV incidence and smaller amplifications for P incidence.

Not only the maximum surface amplification, but also the overall amplification pattern on the surface is affected by the geometry idealization. Figs. 7 and 8 depict the surface amplification patterns for four geometries due to SV and P incident waves, respectively. In these figures, the abscissa is the surface coordinate normalized with respect to the base of the feature b, i.e., the feature is always located between −1 and 1, and the vertical axis is the normalized surface amplification with respect to the flat surface response u^{ff}, whenever $u^{ff} \neq 0$. Notice that the vertical displacement due to a vertically propagating SV, and also the horizontal displacement due to a

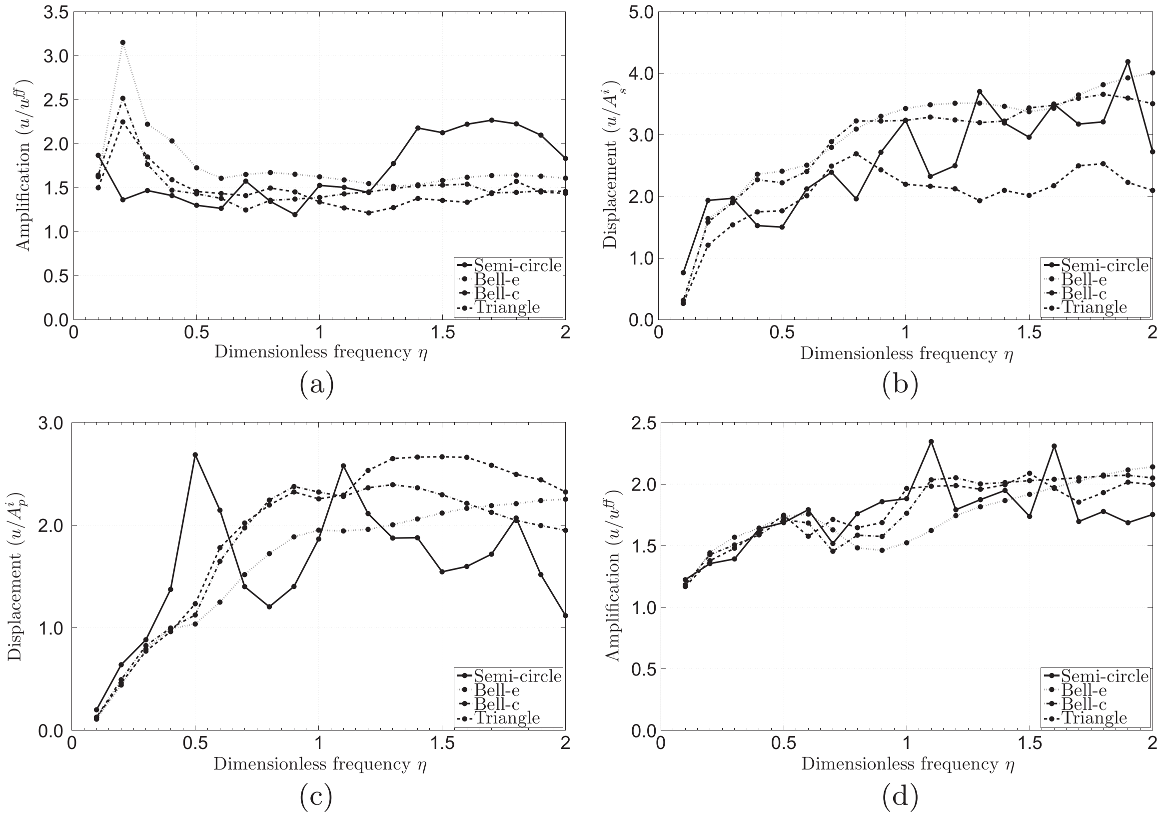

Fig. 5. Comparison of the maximum surface amplifications for four idealized hills due to vertically propagating SV and P incident waves. (a) Horizontal amplification due to SV incidence (b) Vertical displacement due to SV incidence (c) Horizontal displacement due to P incidence (d) Vertical amplification due to P incidence.

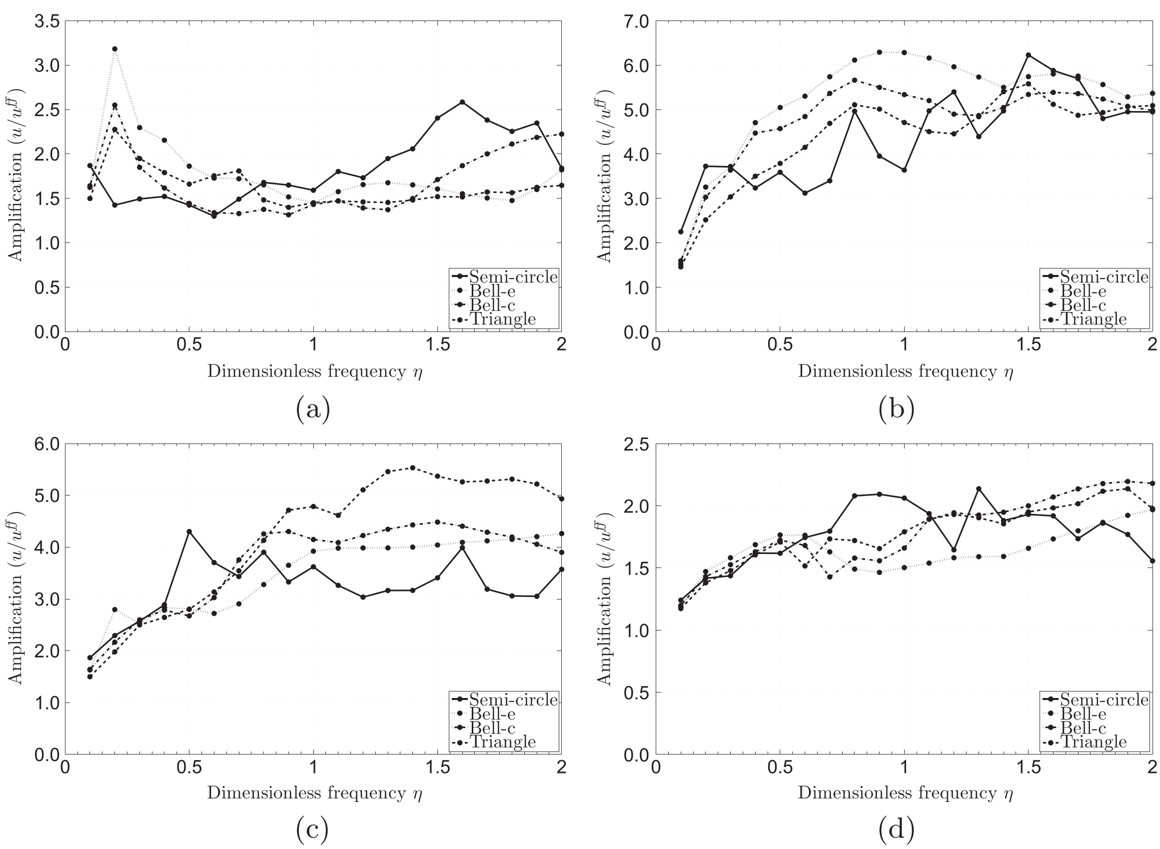

Fig. 6. Comparison of the maximum surface amplifications for four idealized hills due to inclined incidence at $\theta = 15°$. (a) Horizontal amplification due to SV incidence (b) Vertical amplification due to SV incidence (c) Horizontal amplification due to P incidence (d) Vertical amplification due to P incidence.

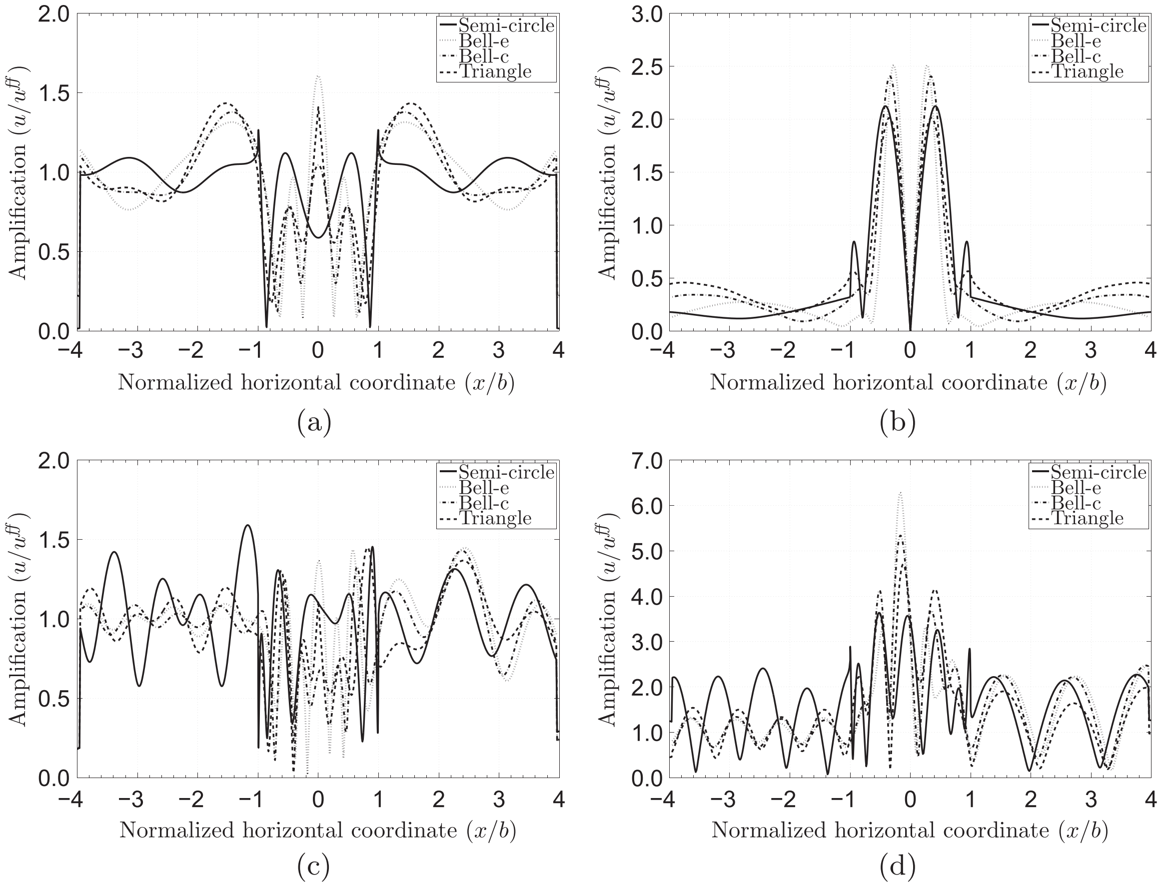

Fig. 7. Amplification pattern on the surface of four idealized hills with Poisson's ratio $\nu = 0.25$ due to SV incidence for two different frequencies (a) x direction, $\eta = 0.6$, $\theta_s = 0°$ (b) y direction, $\eta = 0.6$, $\theta_s = 0°$ (c) x direction, $\eta = 1.0$, $\theta_s = 15°$ (d) y direction, $\eta = 1.0$, $\theta_s = 15°$.

vertically propagating P are zero, on a flat half-space. As a result, in these cases, we plot unnormalized surface displacements.

Fig. 7 indicates that minor changes in the hill's geometry yield remarkable shifts in the amplification pattern on the surface. For example, the semi-circular hill shows larger amplitude oscillations on the flat surface away from the feature, however, the other geometries experience a large amplification mostly within the feature. The amplification patterns of the two bell-shaped hills are quite similar, but are different in magnitude, even though the two hills are close in geometry. The geometry variation also causes the maximum amplifications to occur at different locations on the surface, particularly for the obliquely incident waves. For instance, the largest vertical amplification in the bell-e hill occurs almost at the top of the hill with a magnitude 6.3, yet for the semi-circular hill the amplification is 3.6 and the location shifts away from the mid-point.

The role of geometry variation on the surface amplification pattern is even more noticeable for P incidence as shown in Fig. 8. Not only the patterns and maximum amplifications are different but also the location of the maxima is different. For instance, the maximum displacement for the semi-circular hill occurs closer to the hill top for the horizontal component due to the oblique incidence (Fig. 8(c)), but for other shapes it is closer to the foothill. The horizontal component is more sensitive to the geometry than the vertical component. For example, for $\theta_p = 0°$, the horizontal amplification on the surface of the semi-circular hill at $x/b = 0.90$ is just 0.5, when it is 2.0 for the triangular hill; at the same location, the vertical amplification for both the semi-circular and triangular hills is 1.5.

We conclude that even a small change in the idealized model of the topographic feature has a noticeable effect in both the displacement magnitude and pattern. Thus, the idealization of the real topography should be done carefully so that the computational model remains as close as possible to the physical reality.

4.2. Effects of incident wave frequency

The surface displacement on a flat-surface half-plane domain is independent of the incoming wave frequency, as shown in Appendix A, while in a domain with surface irregularities, the wave frequency (or equivalently the wavelength) plays an important role on surface displacement. The interest in this section is to explore the dependence of the wave amplification on wave frequency through the dimensionless frequency parameter η defined earlier in (5). The influence of the shear wave velocity on the amplification can also be studied using the same parameter η. For example, for a fixed height h, a reduction in η is equivalent to an increase in the incident shear wavelength, which can be interpreted as either a reduction in the frequency or as an increase in the shear wave velocity.

We consider the bell-e hill (see Table 1) with a fixed height $h = 100$ and three different shape ratios $S_r = 15°$, $30°$ and $45°$ in a homogeneous domain with Poisson's ratio $\nu = 0.25$. We plot the normalized maximum amplification on the surface against η for different angles of incidence, irrespective of where the maximum displacement occurs on the surface. The amplification location will be discussed at the end of this section. Notice that the higher η is, the smaller the wavelength is in comparison to the height of the hill.

Fig. 9 displays the maximum amplifications on the surface of a hill with shape ratio $S_r = 45°$ for SV and P incident waves. The horizontal amplifications due to SV incidence are very close for the smaller frequencies (Fig. 9(a)), but as the frequency rises (> 1.0) the amplification reduces and remains between 1.5 and 2.5 for all angles. Fig. 9(b) shows the normalized maximum vertical amplifications due to SV incidence versus the wave frequency for various angles of incidence.

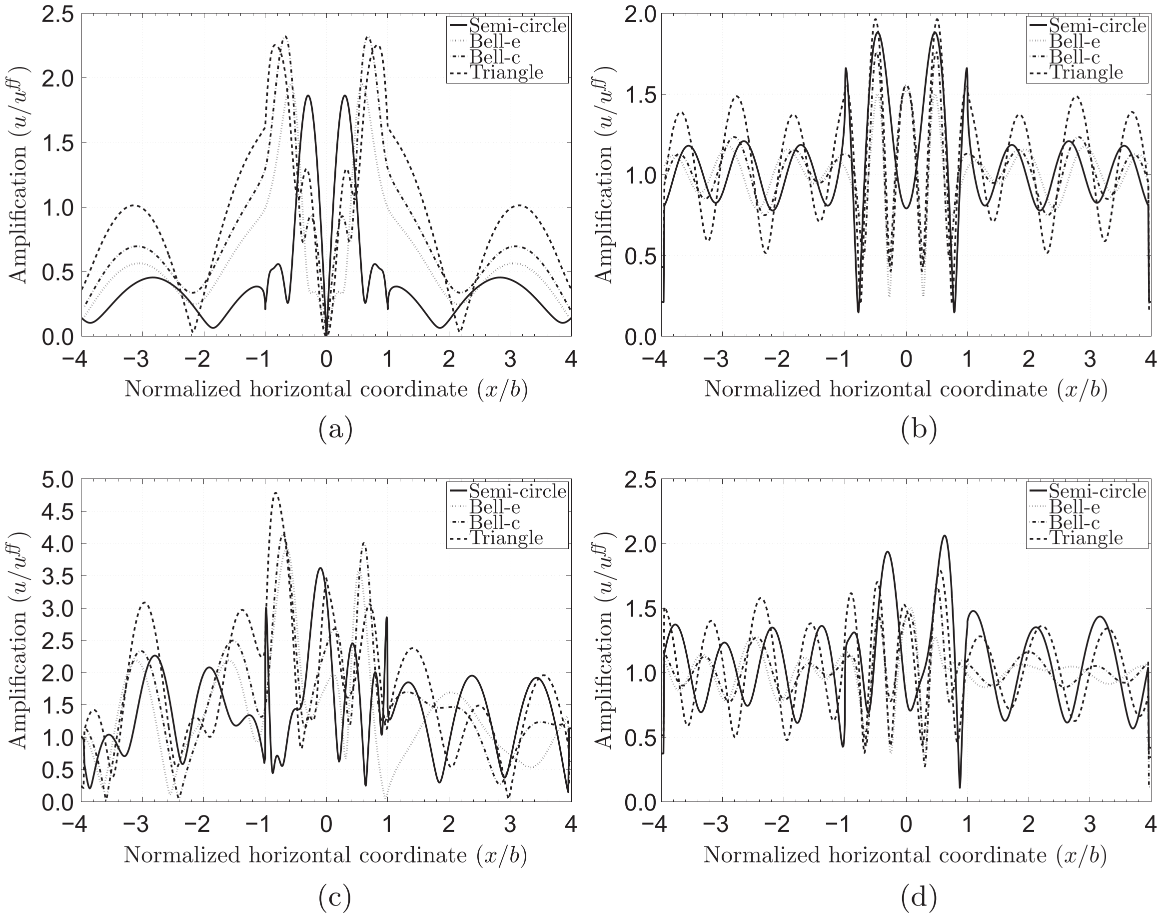

Fig. 8. Amplification pattern on the surface of four idealized hills with Poisson's ratio $\nu = 0.25$ due to P incidence (a) x direction, $\eta = 1.0$, $\theta_p = 0°$ (b) y direction, $\eta = 1.0$, $\theta_p = 0°$ (c) x direction, $\eta = 1.0$, $\theta_p = 15°$ (d) y direction, $\eta = 1.0$, $\theta_p = 15°$.

The vertically propagating SV-wave ($\theta_s = 0°$) is excluded from this graph because the vertical displacement on the surface of a flat domain vanishes for this angle (see Appendix A). We note that the vertical amplifications are much larger than the horizontal ones. For example, the vertical amplification for $\eta = 2.0$ and $\theta_s = 5°$ is 18.2, while the corresponding horizontal amplification is only 1.6. The reason is that the vertical displacement on the flat domain, which we use to obtain the amplification, is much smaller than the horizontal displacement for angles of incidence less than the critical angle (see the free-field solution for a flat half-plane in Fig. A.29).

We remark that the overall amplification tends to reduce steadily as the angle of incidence increases, except for $\theta_s = 35°$. For example, the larger amplification for $\theta_s = 5°$ is 19.0 at $\eta = 1.1$, while the largest amplification for $\theta_s = 30°$ is only 2.0 at $\eta = 1.9$. The reason, as shown in Fig. A.29, is that the vertical displacement on the surface of a flat domain increases as the angle of incidence increases to $\theta_s = 30°$, and then drops quickly for $\theta_s = 35°$. Hence, we expect to see lower amplifications for higher angles of incidence except for $\theta_s = 35°$, which, by contrast, shows a larger amplification. Note again that, similar to the horizontal amplification, amplifications for each angle of incidence are almost constant for all frequencies, except for low frequencies ($\eta < 1.0$).

The horizontal and vertical amplifications for P incidence are plotted in Figs. 9(c) and (d), respectively. Since the horizontal displacement on a flat half-plane is zero for a vertically propagating wave, we do not report it for $\theta_p = 0°$. Similar to the SV incidence case, the horizontal amplification reduces as the angle of incidence rises, but for each angle, particularly for $\theta_p > 25°$, the amplification remains almost constant for frequencies above 2.0, or equivalently for wavelengths half the hill's height or smaller. The largest horizontal amplification is about 12 for $\theta_p = 5°$, which is less than the amplification due to the SV incidence: the vertical amplifications are typically smaller than the horizontal ones. The variation of vertical amplification with frequency is more noticeable in the P incidence case, and becomes less prominent for higher frequencies. The angle of incidence does not seem to be playing a significant role for frequencies $\eta < 2$, but for higher frequencies the amplifications get smaller as the angle of incidence grows.

For a shape ratio $S_r = 45°$, we note that even a small feature, i.e., a small η, causes significant amplification. The topography may amplify incident waves by as much as 19 times, particularly waves propagating at a vertical or close to a vertical incidence. In general, as the angle of incidence increases, the amplification becomes smaller. The only exception is the case of SV incidence at angles close to the critical angle.

We conducted similar experiments for a hill with a shape ratio of $S_r = 30°$. In general, the findings are similar to those drawn for $S_r = 45°$, however, amplifications are overall smaller in comparison to the sharper shape ratio of $S_r = 45°$. In short: the incident waves with smaller angles of incidence experience larger amplifications; the vertical amplification of SV incidence is greater than the horizontal amplification; by contrast, for P incidence, the horizontal amplifications are greater than the vertical ones.

The maximum amplification on the surface of the hill of shape ratio $S_r = 15°$ is depicted in Fig. 10 for P- and SV-wave incidence. We note the lower amplifications in comparison to the other shape ratios. For example, the horizontal amplification due to SV incidence barely reaches 2.0 and the vertical amplification is only 4.6, while the same values for the sharpest hill are 3.4 and 18, respectively. The reason can be attributed to the flatter geometry of this shape ratio that allows the

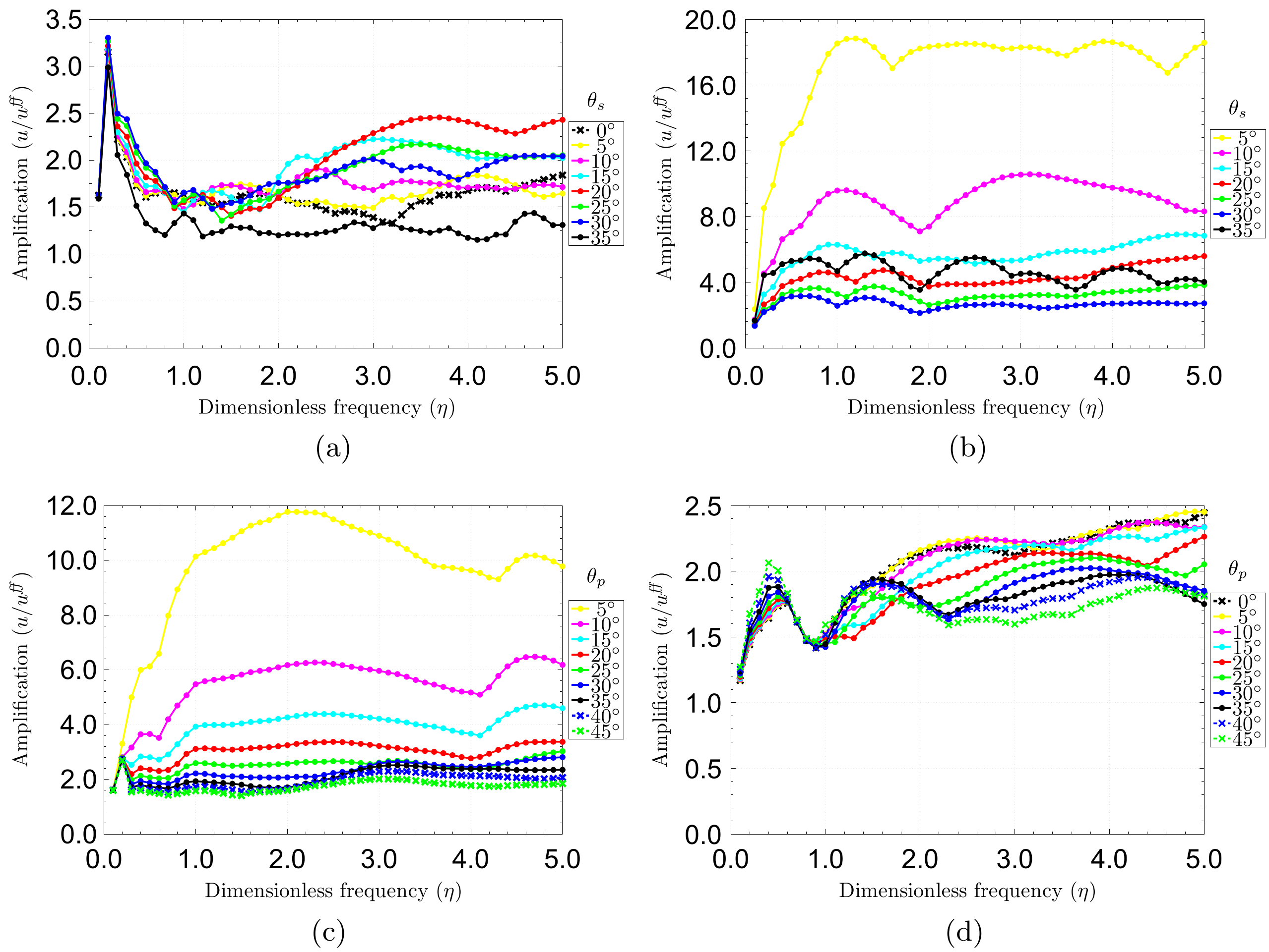

Fig. 9. Maximum amplification on the surface of the bell-e hill of shape ratio $S_r = 45°$. (a) Horizontal amplification due to SV incidence (b) Vertical amplification due to SV incidence (c) Horizontal amplification due to P incidence (d) Vertical amplification due to P incidence.

waves to escape the feature quickly, as opposed to the sharper hill case, where the energy gets trapped within the hill.

Amplifications of P-waves appear to be independent of the wave frequency and stay almost constant for each angle of incidence except for the low frequencies ($\eta < 1.5$). This implies that a flatter hill does not affect incident waves for which the wavelength is several times greater than the hill's height. Another noteworthy pattern for this shape ratio is that the largest vertical amplification is due to the largest angle of incidence $\theta_s = 35°$, while other incidence angles result in substantially smaller amplifications.

In conclusion, wave amplification depends on the incident wave frequency if the frequency is such that the wavelength is comparable to the feature's height, otherwise, if the hill's height is several times greater than the wavelength (large η), the amplification, while significant, is almost frequency independent. Additionally, a sharper hill tends to amplify waves more in comparison to a flatter hill owing to energy trapping within the feature.

4.2.1. Location of the maximum amplification on the surface

In this section, we discuss the maximum amplification location. Fig. 11 displays the location of maximum amplification on the surface of the bell-e hill with shape ratio $S_r = 45°$ for various incidence angles of SV and P incidence. The hill is located between −1 and +1. The location of maximum amplification for SV incidence is primarily within the hill, close but not exactly at the top of the hill, just slightly shifted away toward the sides. This fact is in agreement with the previous observation that wave amplification is due to the trapped energy within the hill. The only major exception here is the SV incidence at $\theta_s = 35°$, where, for several frequencies, the location of the maximum amplification is on the flat surface away from the feature. The location of maximum vertical amplification for P incidence is within the feature. For the horizontal amplification and at low frequencies, the maximum occurs away from the feature, however, as the frequency increases, the location shifts closer to the feature and finally falls within the feature for all frequencies above 2.5. Similar patterns are observed for hills with shape ratios other than $S_r = 45°$.

4.3. Effects of angle of incidence

In this section, we consider the effects of the angle of incidence on the amplification. Toward this end, the scattering of plane waves by the bell-e hill embedded in a homogeneous medium of Poisson's ratio $\nu = 0.25$ is considered. We plot maximum surface amplifications, irrespective of location, against the angle of incidence, ranging from 0° to 35° for plane SV incidence, and from 0° through 45° for plane P incidence, for a few selected frequencies.

Figs. 12(a) and (b) display the maximum horizontal and vertical surface amplifications, respectively, for SV wave against the variation of angle of incidence in a bell-e hill of shape ratio $S_r = 45°$. The horizontal amplification increases for frequencies higher than $\eta = 2.0$, as the angle of incidence increases to 20°, and then drops for higher angles. However, for smaller frequencies, i.e., small feature size in comparison to the wavelength, the amplification is almost independent of the incidence angle. The vertical amplification, on the other hand, falls sharply to 2.5 from 18 as the angle of incidence increases from 5° to 30°, and slightly increases to 4.0 at 35° for almost all frequencies. The

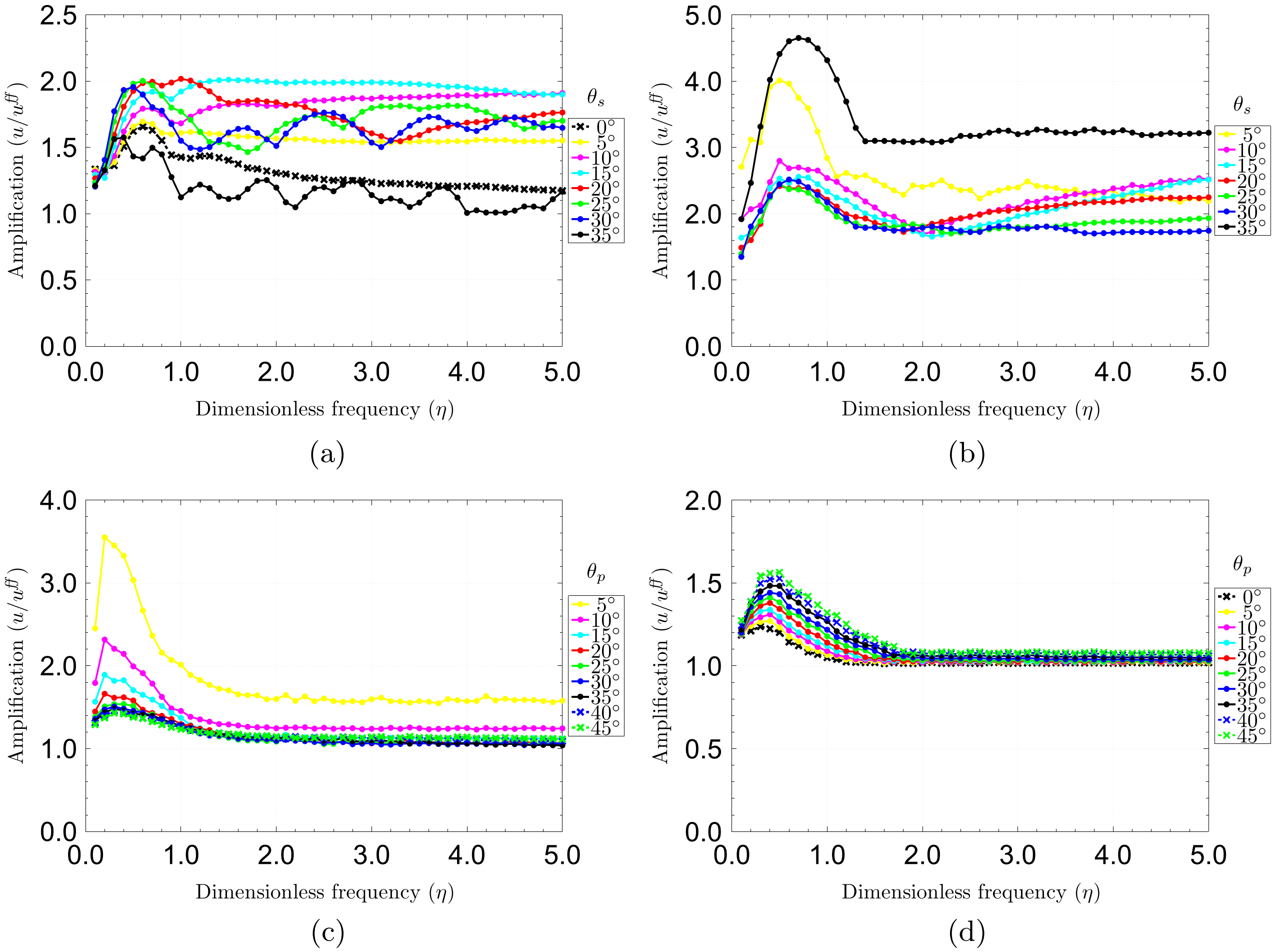

Fig. 10. Maximum amplification on the surface of the bell-e hill of shape ratio $S_r = 15°$. (a) Horizontal amplification due to SV incidence (b) Vertical amplification due to SV incidence (c) Horizontal amplification due to P incidence (d) Vertical amplification due to P incidence.

very low frequencies, e.g., $\eta = 0.1$, are less affected by the incidence angle, similar to the horizontal amplification. In summary, the vertical displacement is more sensitive to the variation of incidence angle for the SV-wave.

According to Fig. 12(c), the horizontal amplification continuously reduces for all frequencies as the angle of incidence increases, except at very low frequencies where it seems to be less affected by the angle of incidence. For example, the amplification reduces from 12 to 1.8 as the angle of incidence increases from 5° to 45° for frequencies higher than 1.5. The vertical amplifications in Fig. 12(d) are not changing much with the angle of incidence, staying almost constant for all angles.

Similar conclusions are drawn for the bell-e hill of shape ratio $S_r = 30°$. In comparison with the steeper hill, $S_r = 45°$, amplifications are smaller for this feature, except for the horizontal amplification of SV incidence, where amplifications are slightly larger for $\theta_s < 15°$. The reason for smaller amplifications might be attributed to the wider character of this shape ratio, which allows the waves to leave the feature with fewer reflections from the sides, thus reducing the likelihood of amplification.

Fig. 13 depicts the maximum surface amplification for the very wide hill of shape ratio $S_r = 15°$. The variation of amplification with respect to the angle of incidence is small and the maximum amplifications for all angles of incidence are significantly smaller than those of the steeper hills.

We note that larger amplifications can be reached for vertically or near-vertically propagating waves. As the angle of incidence increases, the amplification, overall, reduces. The only exception here is the SV incidence, where the amplification rises again just before the critical angle.

4.4. Poisson's ratio effects

We consider the bell-e hill of shape ratio $S_r = 45°$ embedded in a homogeneous domain with mass density $\rho = 2000$ kg/m^3, shear modulus $G = 100$ MPa, and use three Poisson's ratios $\nu = 0.25$, 0.33, and 0.40 to examine the effects of Poisson's ratio on the surface amplification. In this section, we consider the amplification of P- and SV-waves with only two angles of incidence, $\theta = 0°$ and 15°, and the dimensionless frequency ranging from $\eta = 0.1$ to 5.0. Similar to the previous sections, the surface displacements have been normalized with respect to the flat-surface displacements, whenever the latter are non-zero.

We recall that the dimensionless frequency η is normalized with respect to the shear wavelength (see Fig. 5), and, therefore a change in Poisson's ratio, while the shear modulus is fixed, affects only the P-wave velocity/wavelength.

Fig. 14 shows the maximum amplification on the surface of the bell-e hill for vertically propagating P and SV incident waves. The results suggest that for SV incidence, the horizontal amplification and the vertical displacement are not significantly affected by changes in Poisson's ratio, for all frequencies. The reason is that a vertically propagating SV wave reflects from the flat surface as SV only, without any P-wave generated. Thus, as explained earlier in this section, since a change in Poisson's ratio does not alter the SV wave, the amplifications remain the same for all frequencies. Even though, the reflection from the feature leaves a P-wave in the domain, that does not contribute noticeably to the amplification. By contrast, the variation of Poisson's

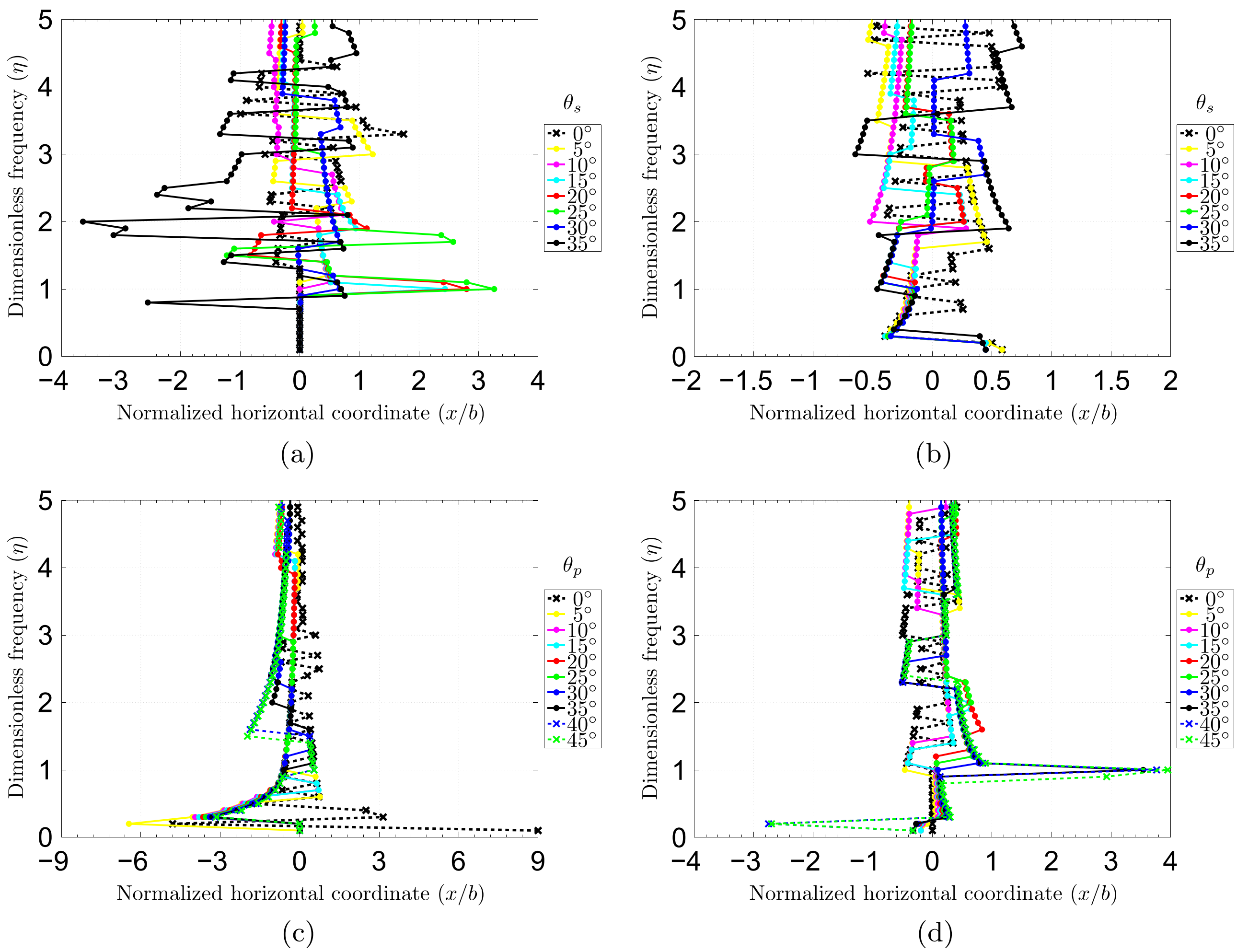

Fig. 11. Location of the maximum amplification on the surface of the bell-e hill with shape ratio $S_r = 45°$ (a) Horizontal amplification due to SV incidence (b) Vertical amplification due to SV incidence (c) Horizontal amplification due to P incidence (d) Vertical amplification due to P incidence.

ratio causes noticeable changes for a P incident wave. The effects of Poisson's ratio are different for horizontal amplification (Fig. 14(c)) than for vertical (Fig. 14(d)): an increase in Poisson's ratio results in a larger amplification for the horizontal component and a smaller amplification for the vertical component. For example, the horizontal amplification for $\eta = 3.0$ increases from 2.0 to 2.5 as ν changes from 0.25 to 0.4, while the vertical amplification reduces from 2.2 to 1.6.

In Fig. 15, we plotted the maximum surface amplification on the bell-e hill due to the plane P- and SV-waves, propagating at the incidence angle of 15°. The apparent change, compared to the vertically propagating waves, is the variation of the vertical amplification with Poisson's ratio for SV incidence (Fig. 15)(b). For example, the amplification for frequency $\eta = 3.0$ is 10.1 for Poisson's ratio $\nu = 0.40$, while the amplification for $\nu = 0.25$ is 5.1, however, for the same frequency the vertical amplifications are about 3.8 for all Poisson's ratios for a vertically propagating SV-wave (Fig. 14(b)). The reason is that an oblique SV-wave results in a P-wave reflection from the surface that will have a different wavelength as Poisson's ratio varies. Notice as well that the vertical component of the P wave is more prominent compared to the horizontal component, consequently, the variation of amplification with Poisson's ratio is more significant for the vertical amplification for SV incidence. For the oblique P incidence, the amplification pattern remains the same as the vertical propagation in a way that a rise in Poisson's ratio will lead to a climb in the horizontal amplification and a drop in the vertical ones. The Poisson's ratio variation affects oblique waves more strongly than vertical waves. For instance, the horizontal amplification of the oblique P wave for frequency $\eta = 3$ increases from 4.1 to 7.7 as Poisson's ratio increases from 0.25 to 0.4, whereas for the vertical wave the same values are 2.0 and 2.51, respectively.

We remark that the total amplification reduces as Poisson's ratio increases for the P incidence, particularly for frequencies above $\eta = 1.5$, because the vertical surface displacement is larger than the horizontal one. Consequently, even though the horizontal amplification increases sharply, the vertical amplification, which has a larger amplitude, drops, and the result is a total surface amplification reduction. This amplification reduction is expected because as Poisson's ratio increases, the wavelength of the P incidence increases; hence, the feature appears smaller to the incoming wave. The amplification exhibits minor changes for lower frequencies as Poisson's ratio varies, because, in general, the feature is almost invisible to low-frequency incident waves. The trend is quite different for the SV incidence where an increase in Poisson's ratio results in a slightly larger total amplification, because the horizontal displacement, which is greater in magnitude, exhibits a minor change, while the vertical component is amplified. Yet, the total variation remains small, because the magnitude of the vertical component is small.

The variation of Poisson's ratio induces modifications in the amplification pattern on the surface of the domain. To show these effects, we plot the amplification patterns for three different Poisson's ratios in Figs. 16 and 17 due to oblique SV and P incident waves, respectively, for a dimensionless frequency $\eta = 2.0$. The horizontal and vertical amplifications caused by the SV incident wave for all three Poisson's ratios are very similar, except at the hilltops. The difference is

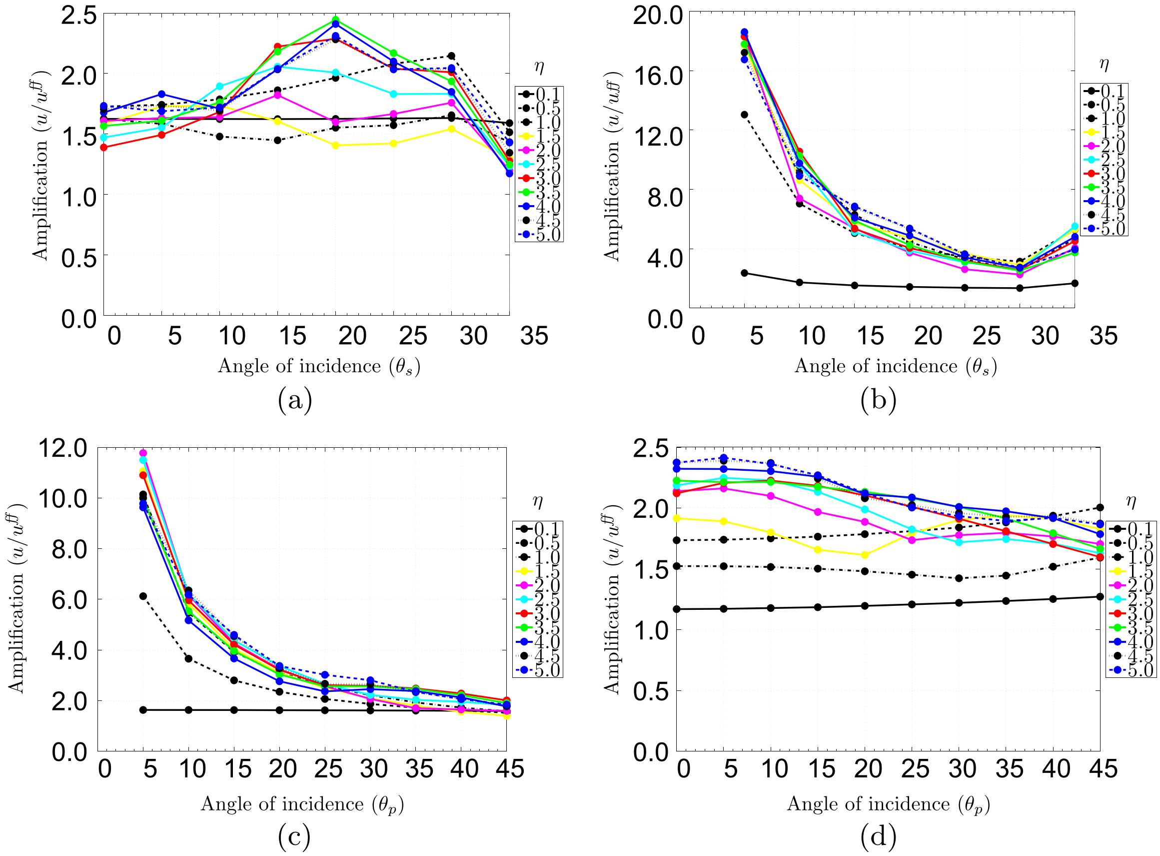

Fig. 12. Maximum amplification on the surface of the bell-e hill of shape ratio $S_r = 45°$. (a) Horizontal amplification due to SV incidence (b) Vertical amplification due to SV incidence (c) Horizontal amplification due to P incidence (d) Vertical amplification due to P incidence.

more significant for the vertical amplification. The shift in the amplification is more prominent for the incident P-wave. The difference between the patterns is significant within the feature, yet, mostly the same away from the feature on the flat surface.

4.5. Spatial amplification patterns

In this section, we report the effects the presence of a hill has on the displacement pattern on the surface surrounding the topographic feature.

Figs. 18(a) and (b) show the amplification on the surface of the bell-e hill with shape ratio $S_r = 45°$ for a vertically propagating SV incidence with frequencies $\eta = 0.6$ and $\eta = 2.0$, respectively. The horizontal axis is normalized with respect to the base of the hill such that the feature is located between −1 and +1. We only normalize the horizontal amplification with respect to the free-field solution in a flat domain, because the vertical component in the flat domain is zero. The vertical displacement within the feature is quite significant, 2.5 times of the amplitude of the incident wave for $\eta = 0.6$ and 4.0 times of the amplitude of the incident wave for $\eta = 2.0$. However, the amplification on the flat surface around the feature is negligible. More interestingly, stationary points, where the displacement is zero or close to zero, exist on the surface because of the destructive interference of plane and surface waves. The number of stationary points increases as the frequency increases. Overall, the strongest amplification occurs mostly within the feature, while it oscillates around one away from the feature.

The surface amplifications for the oblique SV incidence with angle of incidence 35° are plotted in Figs. 19(a) and (b) for frequencies $\eta = 0.6$ and $\eta = 1.0$, respectively. The oblique incident wave enters the domain and impinges upon the feature from the left (negative x). Accordingly, the amplification on the flat surface on the left side of the feature exhibits a smaller amplification, while the flat surface on the right side experiences a large amplification. For example, for $\eta = 0.6$, the maximum vertical amplification is only 1.6, whereas it is 2.6 on the right side. For $\eta = 1.0$, the difference is even more prominent, 1.7 versus 3.6. Note, however, the maximum amplification occurs on the left slope of the feature. In summary, the presence of a hill in the propagation path of an oblique SV incident wave results in surface amplification on the hill, and on the forward scatter region of the feature. We conducted similar experiments with oblique P-waves and reached analogous conclusions.

Thus far, we only focused on the amplification effects that topography causes on the surface displacement. Indeed, in some cases, de-amplification may also develop. For example, the surface amplification due to the propagation of P-wave with angle $\theta_p = 45°$ in a hill with shape ratio $S_r = 45°$ shows de-amplification at some locations (see Fig. 20). The horizontal amplification for $\eta = 0.6$ de-amplifies within the entire feature to the extent that it reduces to 0.2 at one point. A remarkable de-amplification of the vertical component occurs as well on the left side of the hill. For the higher frequency, as shown in Fig. 20(b), de-amplification is less prominent.

Fig. 21 depicts the surface amplification on the surface of a hill with shape ratio $S_r = 15°$ due to SV incidence. A flat hill, as expected, leads to small amplifications in comparison to a steep hill. For the vertically propagating SV incidence shown in Fig. 21(a), the horizontal amplification oscillates rapidly around one, while the magnitude barely reaches to 1.25. The vertical displacement is almost negligible. For an oblique SV incidence, as shown in Fig. 21(b), with an angle $\theta_s = 35°$, no amplification occurs on the flat surface on the left side of the feature where the wave hits the domain first, however, there is a significant amplification on the feature and also on the forward scatter region. By contrast, the horizontal component experiences a de-amplification within and away from the feature on the flat surface to the right.

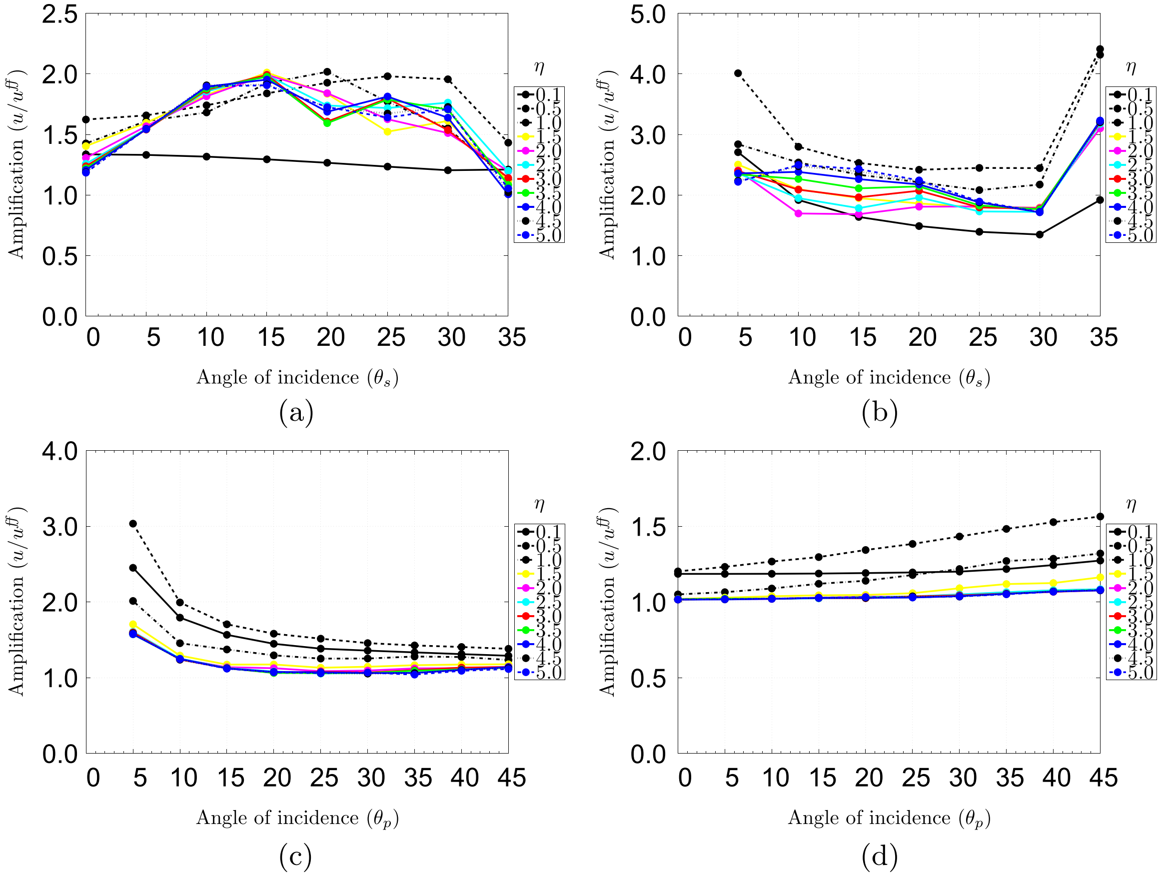

Fig. 13. Maximum amplification on the surface of the bell-e hill of shape ratio $S_r = 15°$. (a) Horizontal amplification due to SV incidence (b) Vertical amplification due to SV incidence (c) Horizontal amplification due to P incidence (d) Vertical amplification due to P incidence.

5. Parametric study on valleys

In this section, we report parametric studies on the effect valleys have on the amplification/de-amplification of seismic waves. We use a two-dimensional linear elastic, homogeneous half-plane with Poisson's ratio $\nu = 0.25$, mass density $\rho = 2000\ \mathrm{kg/m^3}$, and shear modulus $G = 100$ MPa. The only shape ratio that we consider for this section is $S_r = 45°$, where b is the base and h is the depth of the valley, as depicted in Fig. 3(b). The dimensionless frequency for the incident wave is again defined as $\eta = h/\lambda_s$, which is the ratio of the valley's depth to the shear wavelength.

5.1. Effects of feature's geometry

We use again the same four geometry functions defined previously in Table 1, but flip the geometry with respect to the x axis to idealize valleys. We use a single dimensionless frequency $\eta = 1.0$, and two angles of incidence $\theta = 0°$ and 15° for P- and SV-waves.

Fig. 22 displays the surface displacement, normalized with respect to the free-field solution, whenever the displacement is non-zero, for vertically propagating SV- and P-waves. The horizontal axis of this figure runs along the surface, and is normalized with respect to the base of the valley such that the valley is always located between −1 and +1. The maximum horizontal amplification due to SV wave occurs on the flat surface away from the valley; it is around 1.5 for all four geometries, with the triangular valley showing the largest amplification. The difference between the amplification pattern of the various geometries is more interesting within the feature: the semi-circular valley exhibits a small amplification, whereas all other geometries show de-amplification. Conversely, the semi-circular valley shows the least vertical amplification (Fig. 22(b)) within the valley, but the largest on the flat surface, i.e., 2.8 versus 1.95. In terms of the surface pattern, all geometries are quite similar with the exception of the semi-circular valley, which shows a sharp drop and rise at the valley ends, for both horizontal and vertical displacements.

The contribution of the valley idealization is more prominent for the P incidence as shown in Figs. 22(c) and (d). The amplification patterns for the various geometries are relatively different, with the bell-e valley showing the largest amplifications, both horizontal and vertical, while the smallest amplification is associated with the triangular valley. Seemingly, for P- and SV-waves, the amplification within the valley is less than the amplification on the flat surface, and at a few locations de-amplification occurs.

Fig. 23 shows the amplification pattern on the surface of the four geometries for oblique incident waves with $\theta = 15°$. Similar conclusions can be drawn here. Among them is the apparent difference between the amplification of the semi-circular valley with the bell-shaped valleys, mainly because of the sharp corners of this geometry.

In summary, small changes in the geometry of the valley result in significant changes in the surface pattern and in the maximum amplification. Overall, it is very likely that amplification on the flat surface away from the feature is larger than the amplification within the valley. Clearly, for higher wave frequencies, the difference between the amplification of various geometries is bigger. Hence, when idealizing valleys, it is important that the computational geometry stays as close to the physical domain as possible for accurate predictions of the amplification patterns.

5.2. Effects of incident wave frequency

We study parametrically the dependence of the valleys' surface amplification on the dimensionless frequency parameter η. Figs. 24(a)

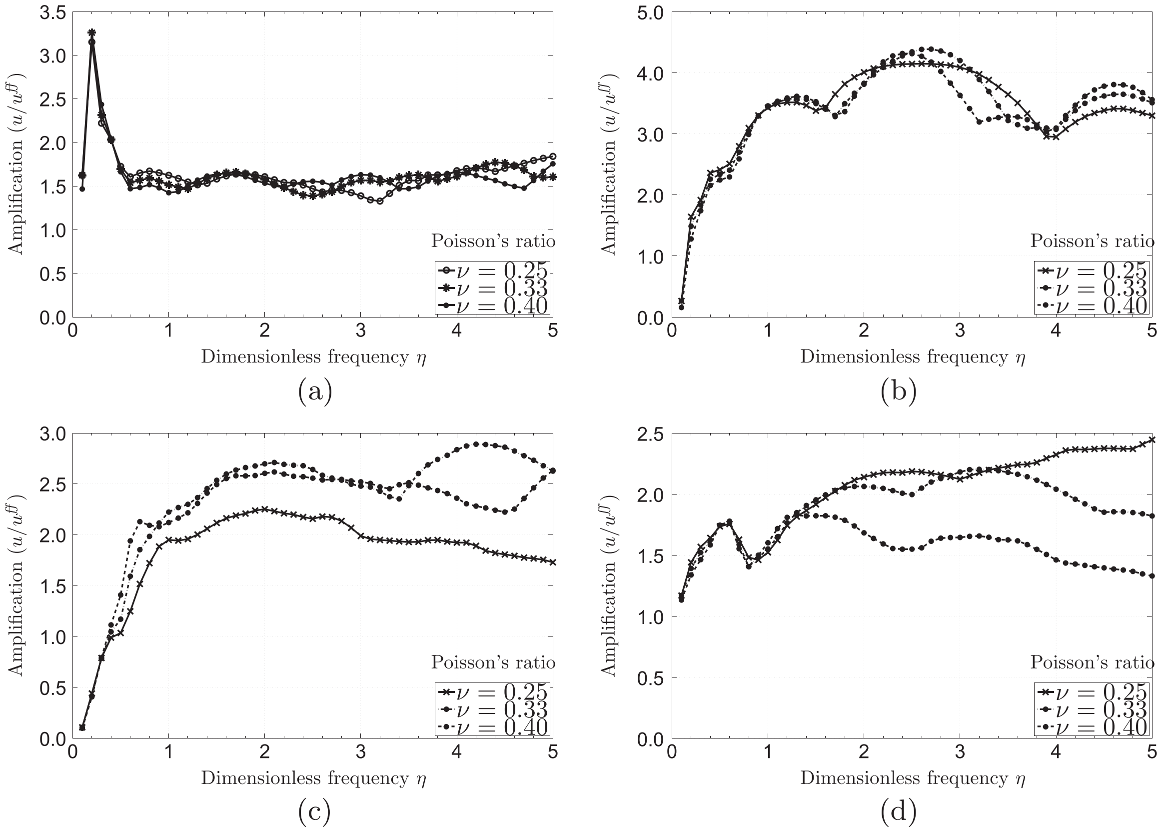

Fig. 14. Maximum amplification on the surface of a bell-e hill of shape ratio $S_r = 45°$ due to vertically propagating waves. (a) Horizontal amplification due to SV incidence (b) Vertical amplification due to SV incidence (c) Horizontal amplification due to P incidence (d) Vertical amplification due to P incidence.

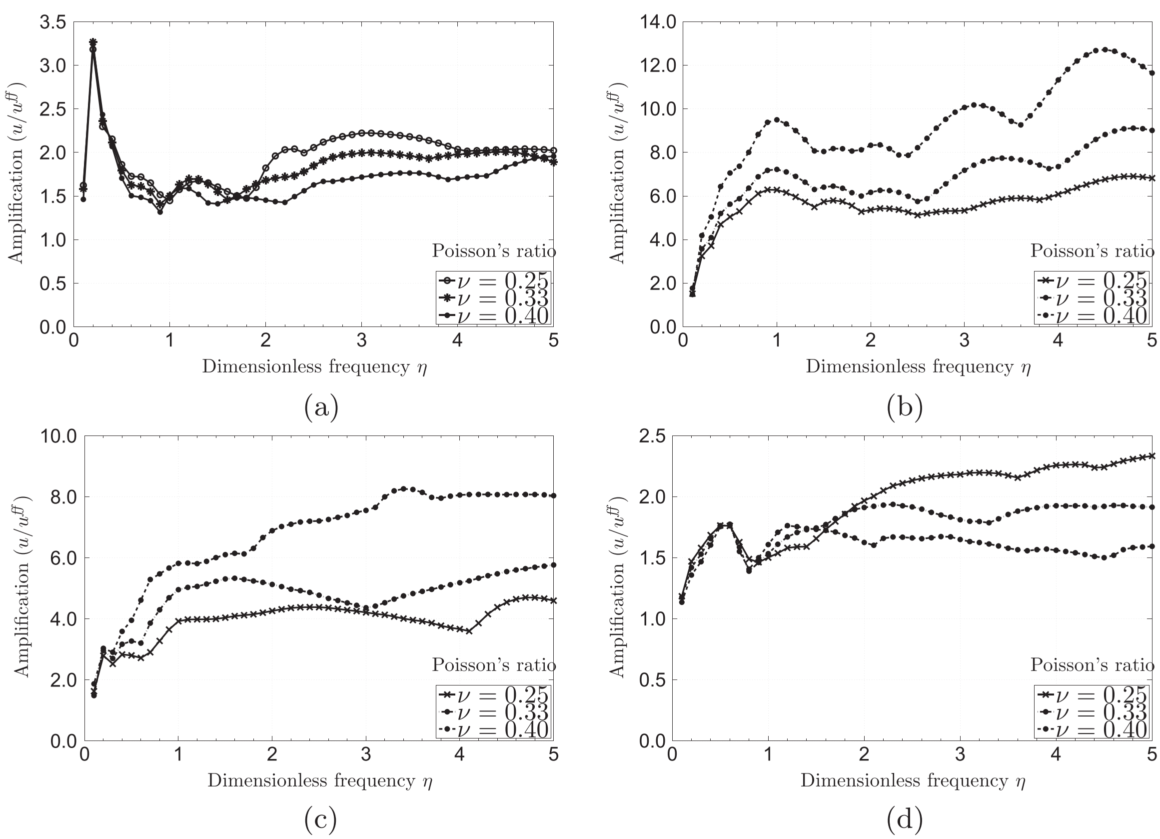

Fig. 15. Maximum amplification on the surface of the bell-e hill of shape ratio $S_r = 45°$. The angle of incidence is 15°. (a) Horizontal amplification due to SV incidence (b) Vertical amplification due to SV incidence (c) Horizontal amplification due to P incidence (d) Vertical amplification due to P incidence.

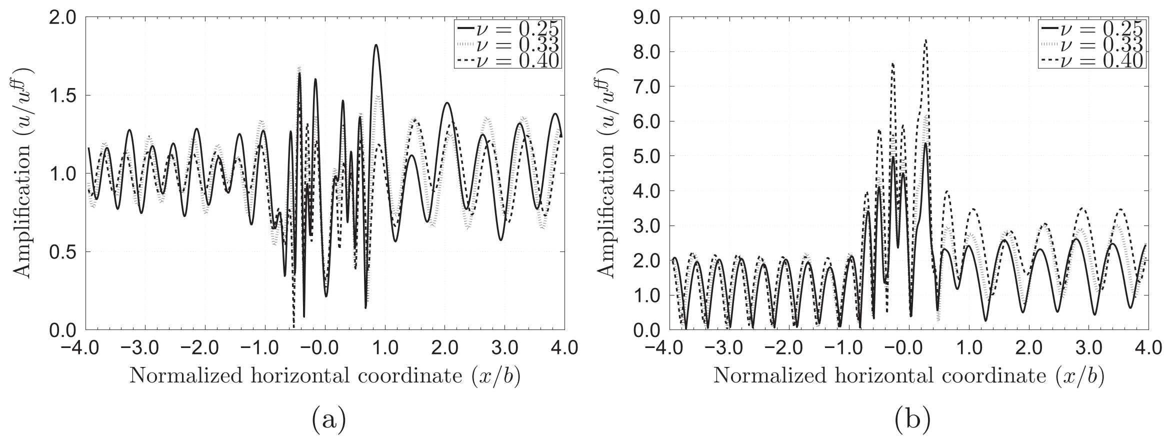

Fig. 16. Amplification pattern on the surface of the bell-e hill of shape ratio $S_r = 45°$ results from an inclined SV incident wave of angle $\theta_s = 15°$ for different Poisson's ratios. The dimensionless frequency is $\eta = 2.0$. (a) Horizontal amplification (b) Vertical amplification.

and (b) show the maximum horizontal and vertical amplification, respectively, on the surface of the bell-e valley of shape ratio $S_r = 45°$ against the frequency for SV incidence. We note that the amplification is almost constant for frequencies above $\eta = 1.5$ for all angles of incidence, which implies that the amplification depends on the frequency if the incident shear wavelength is almost the same size as the valley's depth, otherwise, if the wavelength is more than 1.5 times the depth of the valley, the presence of the valley amplifies the wave at each angle of incidence with the same magnitude. The only exception is the vertical amplification of SV incidence at angle $\theta_s = 5°$, where the amplification reduces to 7.5 at $\eta = 2.90$ from its peak value 11.6, and increases again to 9.6 at $\eta = 5.0$. Overall, analogous to the hill topography, the vertical amplifications are greater than the horizontal ones, though they are, in general, smaller than the amplifications caused by hills.

P incidence results in a larger horizontal amplification in comparison to the vertical amplification, as depicted in Figs. 24(c) and (d). Overall, for frequencies above $\eta = 0.5$, the horizontal and vertical amplifications reduce slightly as the frequency increases. Notice that the vertical amplifications for all angles are quite the same, however, the horizontal amplifications are well separated in a way that the higher angles yield smaller amplifications. In conclusion, surface amplification caused by a valley is less sensitive to the frequency in comparison to the hill topography.

5.2.1. Location of the maximum amplification on the surface

Fig. 25 depicts the location of the maximum displacement for P- and SV- waves on the surface of a half-plane, including the valley. The maximum horizontal amplification due to SV incidence is outside of the valley, mostly for lower angles of incidence and frequencies, and gradually moves toward the valley as the frequency increases. This trend is, in general, the same for the vertical amplification. For the P incidence, the location of the maximum horizontal and vertical amplifications is outside of the valley. As the frequency increases, the location moves toward the valley, but still remains outside for the majority of the cases. We note that in most cases, the maximum amplification occurs away from the topographic feature, which implies that the presence of a valley results in an amplification on the flat surface away from the feature and that the valley itself may even experience a de-amplification.

5.3. Effects of angle of incidence

Fig. 26 illustrates the effects of incidence angle on the surface amplification of the bell-e valley of shape ratio $S_r = 45°$ for a few selected frequencies. The horizontal amplification due to SV incidence and the vertical amplification due to P incidence seem to be independent of the angle of incidence, whereas the other components are substantially affected by this parameter. For example, the vertical amplification of SV incidence reduces drastically as the angle of incidence increases up to $\theta_s = 30°$, and increases only slightly for higher angles. The reason, as we discussed earlier, is that the vertical displacement of SV incidence on the surface of a flat homogeneous half-plane, used to compute the amplification, is minimum at $\theta_s = 30°$ and rises to the maximum amount at the critical angle (see Fig. A.29). The horizontal amplification of P wave is steadily decreasing as the

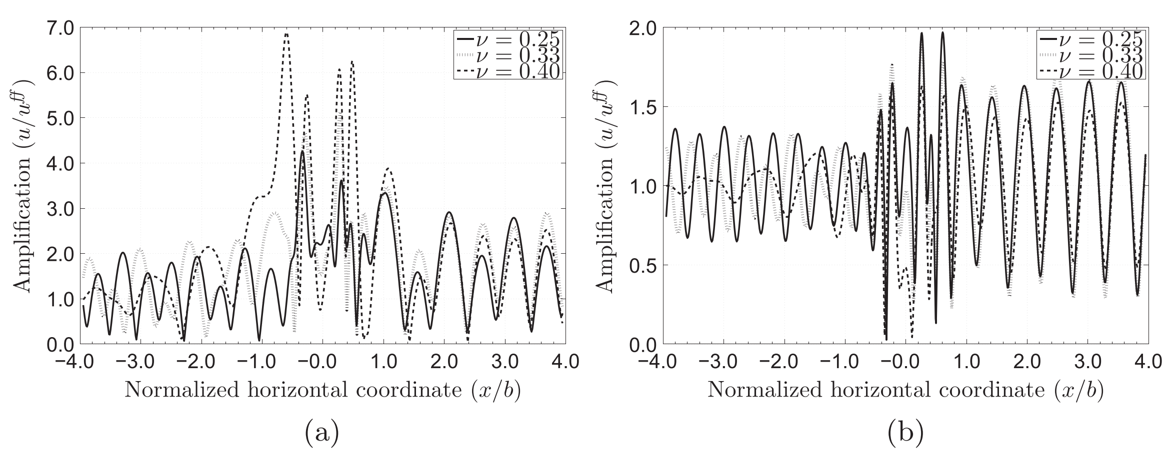

Fig. 17. Amplification pattern on the surface of the bell-e hill of shape ratio $S_r = 45°$ results from an inclined P incident wave of angle $\theta_p = 15°$ for different Poisson's ratios. The dimensionless frequency is $\eta = 2.0$. (a) Horizontal amplification (b) Vertical amplification.

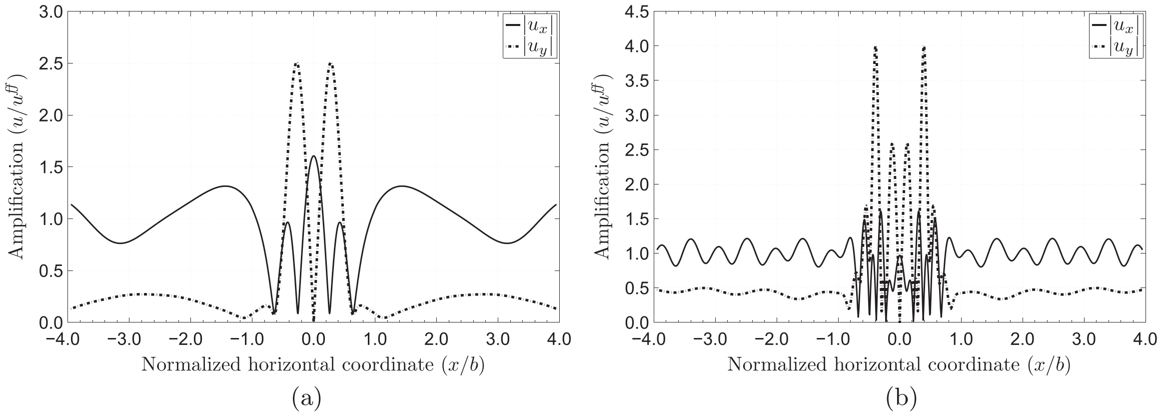

Fig. 18. Amplification pattern on the surface of the bell-e hill of shape ratio $S_r = 45°$ for a vertically propagating SV-wave. (a) (b) .

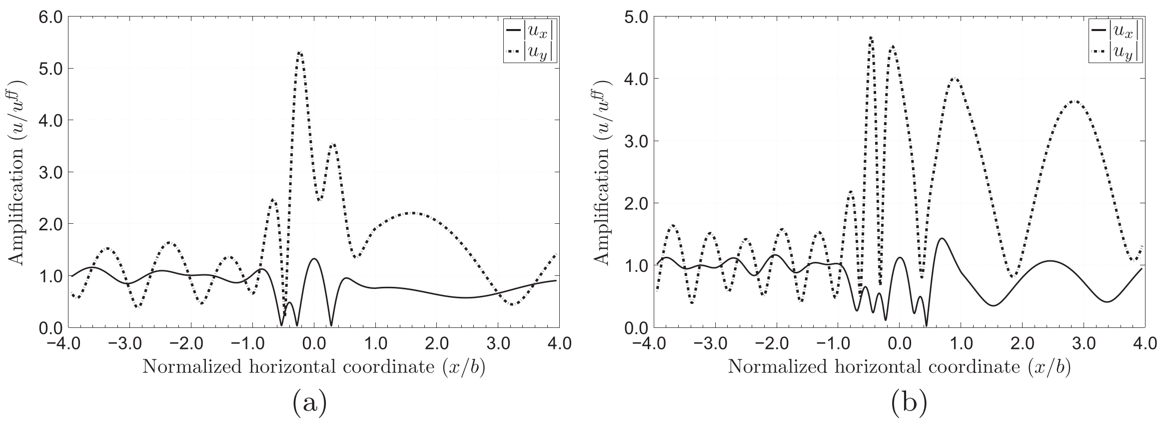

Fig. 19. Amplification pattern on the surface of the bell-e hill of shape ratio $S_r = 45°$ for the oblique SV-wave with angle $\theta_s = 35°$. (a) $\eta = 0.6$ (b) $\eta = 1.0$.

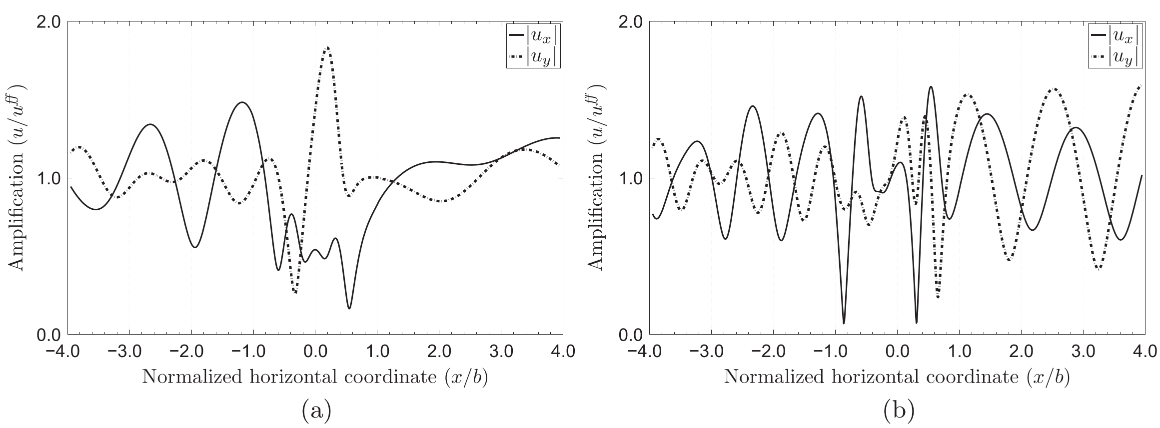

Fig. 20. Amplification pattern on the surface of the bell-e hill of shape ratio $S_r = 45°$ for the oblique P-wave with angle $\theta_p = 45°$. (a) (b) .

angle of incidence increases to the point that the amplifications for all frequencies at $\theta_p = 45°$ are almost identical. We add that the vertical displacement due to the SV incidence and the horizontal displacement due to the P incidence are fairly small in comparison to the other components; hence, even though the amplification of these components seems to be prominent, the total amplification is still not that big. We also note that the dependence of the amplification on the angle of incidence reduces as the frequency of the incident wave becomes smaller.

5.4. Spatial amplification patterns

The presence of a feature induces substantial changes on the amplification pattern not only on the surface of the feature but also on the flat surface away from it. In this section, we study the effect the presence of the valley has on the surface patterns for a few cases.

Fig. 27(a) shows the amplification pattern on the surface of a bell-e valley of shape ratio $S_r = 45°$ due to a vertically propagating SV incidence with $\eta = 1.0$. The horizontal component is de-amplified on the entire surface of the valley, but it is amplified on the flat surface away from the feature. This pattern is the opposite of the hill's pattern, where the maximum amplification normally occurs on the surface of the hill. The reason is that the valley de-focuses the energy by diffracting waves away from the feature. The vertical displacement in this case is due to the reflection of waves from the valley, since a vertical SV incidence does not develop any vertical displacement on a flat half-plane. The amplitude of the vertical component is quite large in comparison to the amplitude of the incoming SV incidence and

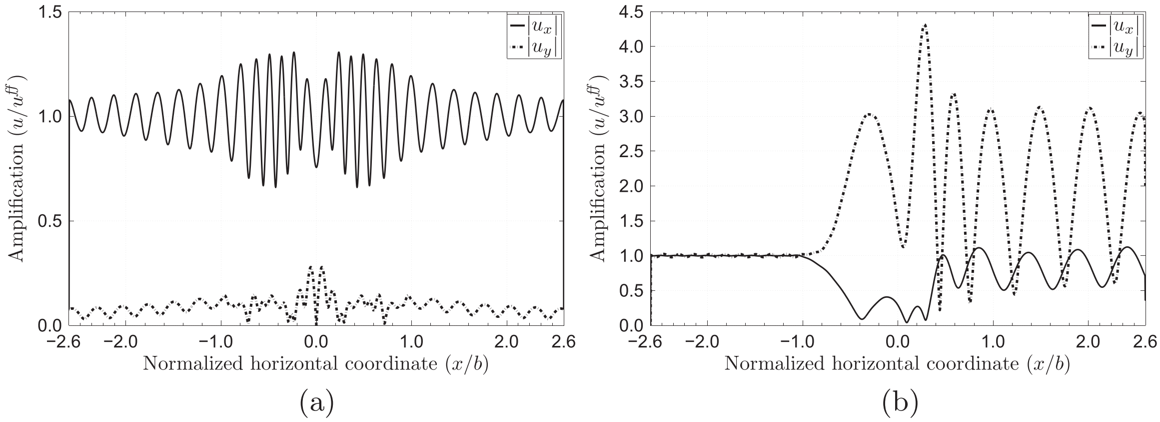

Fig. 21. Amplification pattern on the surface of the bell-e hill of shape ratio $S_r = 15°$ due to the plane SV wave (a) $\theta_s = 0°$, $\eta = 2.0$ (b) $\theta_s = 35°$ and $\eta = 1.0$.

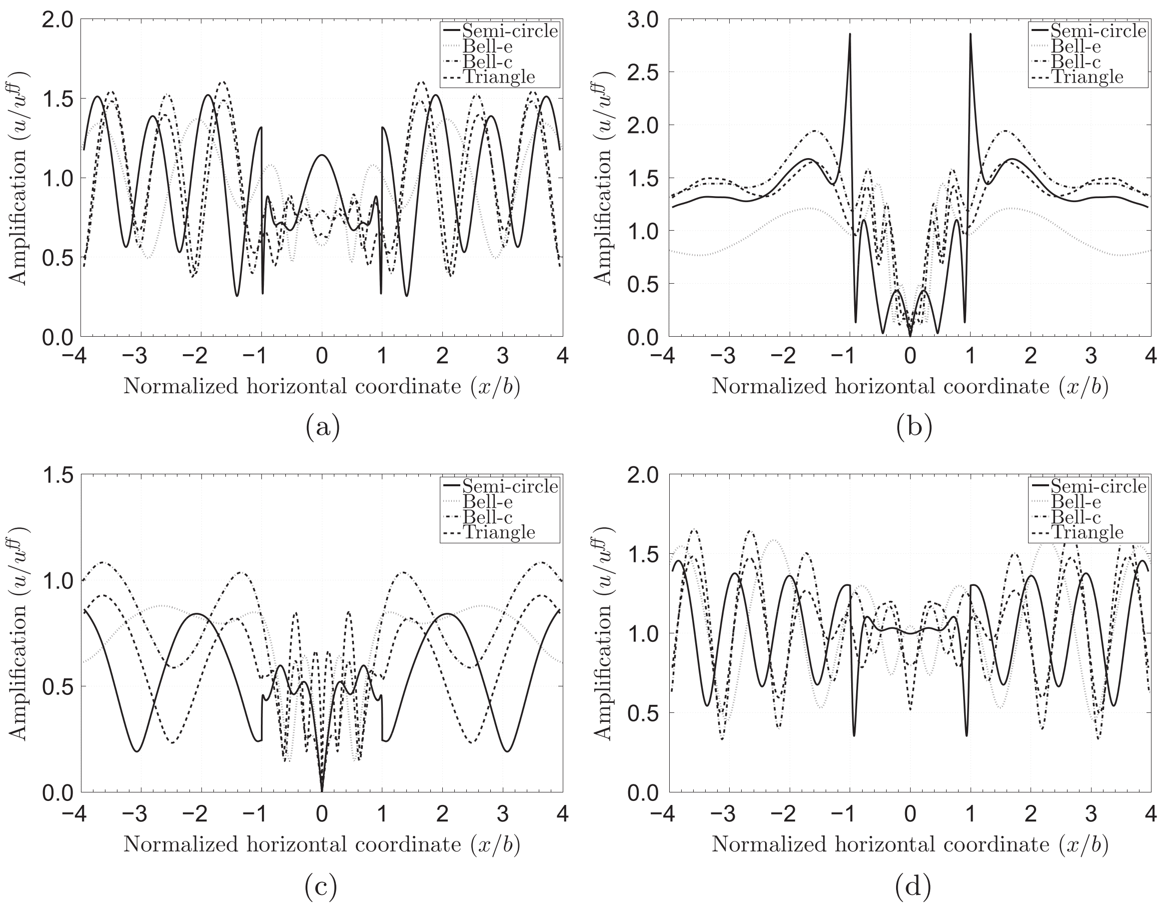

Fig. 22. Amplification pattern on the surface of four idealized valleys due to vertically propagating waves. (a) Horizontal amplification due to SV incidence (b) Vertical amplification due to SV incidence. (c) Horizontal amplification due to P incidence (d) Vertical amplification due to P incidence.

reaches its largest value next to the edge of the valley on the flat surface.

Fig. 27(b) depicts surface amplification for P incoming waves with $\eta = 2.0$. The horizontal amplification, which is generated by the reflection of waves from the valley, is maximum outside the feature and has the smallest values within the valley. The vertical amplification on the surface of the valley is negligible, while away from the valley it increases remarkably. Since the frequency of the incident wave is twice the frequency of the previous case, we expect to see more ripples in the solution.

Fig. 28 displays the amplification pattern for obliquely incoming plane P and SV waves with $\theta = 15°$. The amplification is larger on the flat surface, and de-amplification occurs within the valley, particularly in the x direction. Moreover, significant amplification occurs on both sides of the valley, which implies that the presence of a canyon drastically changes the displacement everywhere on the surface of the half-plane.

6. Conclusions

This paper provided a synopsis on the problem of amplification of harmonic plane P- and SV-waves by idealized topographic feature in a semi-infinite linear elastic, homogeneous two-dimensional half-plane.

Overall, the feature's geometry and its relation to the characteristics of the propagating waves affect decisively the severity of the motion amplification in terms of magnitude and location.

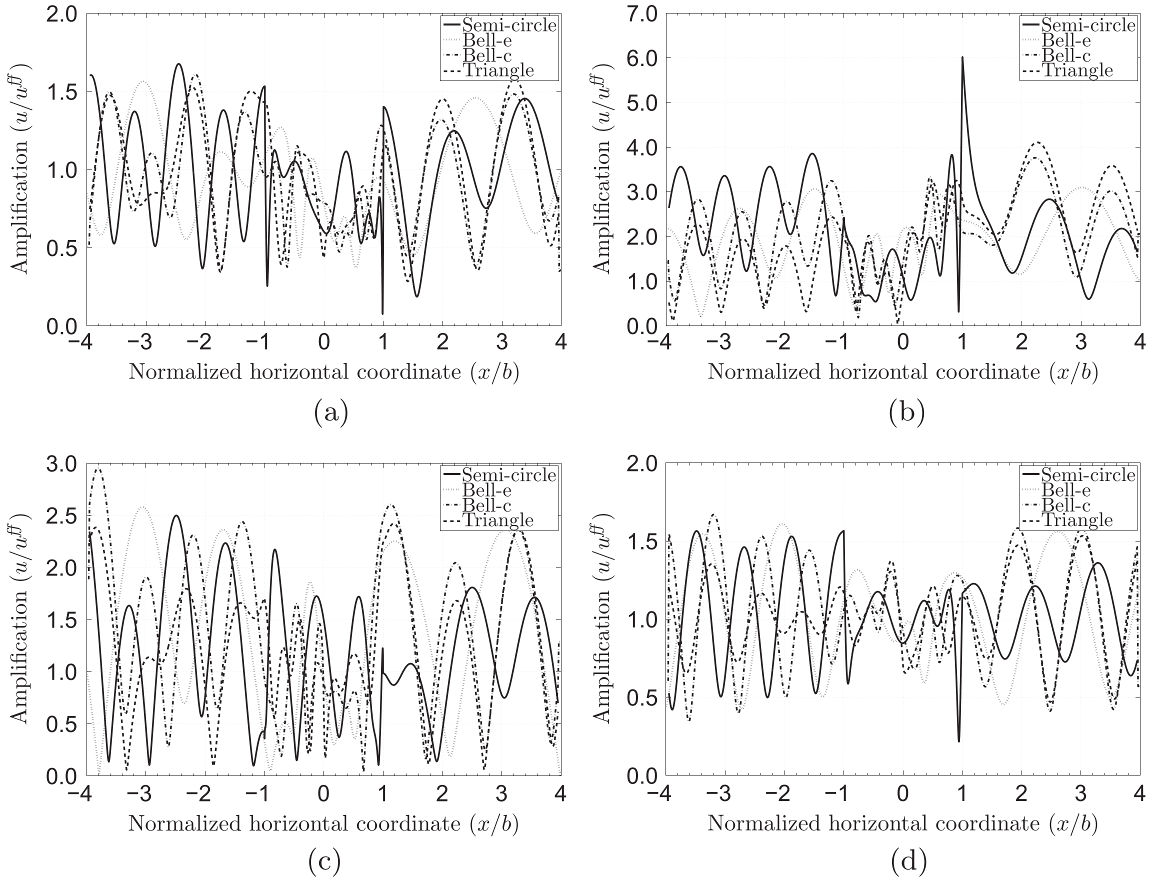

Fig. 23. Amplification pattern on the surface of four idealized valleys. The angle of incidence is $\theta = 15°$. (a) Horizontal amplification due to SV incidence (b) Vertical amplification due to SV incidence (c) Horizontal amplification due to P incidence (d) Vertical amplification due to P incidence.

For events characterized by frequencies resulting in wavelengths longer than a characteristic dimension of the topographic feature, the feature appears nearly transparent to the incoming wave, and the resulting surface motion pattern is almost unaffected by the presence of the feature. But, in all other cases, a complex motion pattern emerges, resulting in significant amplification.

As expected, the strongest amplification is observed within the topographic feature, owing to the constructive interference of both body and surface waves inside and on the surface of the feature. But, the occurrence of strong amplification away from the feature cannot be excluded, as special cases reported herein demonstrate.

An interesting observation emerging from the present study refers to the importance of maintaining as faithful a geometric representation of the physical terrain as is possible, especially in light of the growing reliance on digital elevation data: two fairly close geometries may result in significantly different amplification patterns, as the numerical studies demonstrated.

We also reported on amplification patterns related to idealized valleys: overall, the amplification is weaker when dealing with terrain depressions than with proud topographic features.

Specific observations include:

- The approximation of a topographic feature's geometry affects the amplification in the SV incidence case, regardless of the angle and frequency of the incident wave. By contrast, for P incidence, the amplification at low frequencies is less affected by geometric variations.
- The surface pattern on a hill is significantly affected by the feature's geometry. There are noticeable differences in the amplification pattern between the semi-circular feature, and any of the other three considered geometries. Differences can be observed even between the triangular feature and any of the two bell-shaped circumscribing geometries, both within the feature, as well as on the flat surface exterior to the feature. Differences in the overall amplification pattern between the two bell-shaped geometries are less pronounced, but become significant in the region within the feature, indicating again the importance of geometric representation.
- In general, for low frequencies, or equivalently, for incident wavelengths that are several times the size of the feature's height, the effect of the feature's geometry tends to diminish, leading to smaller amplification values.
- The angle of incidence tends to impact more the amplification for higher frequencies. For very low frequencies ($\eta < 0.5$), which are tantamount to a small feature in comparison to the incident wavelength, the angle of incidence does not change the amplification significantly.
- The interplay between the angle of incidence and the feature's geometry suggests that when waves become trapped within the feature in such manner that a constructive interface pattern is developed, the amplification can become large. By contrast, when the feature is wide enough, reflected waves from the sides of the hill leave the feature without being trapped, resulting in smaller amplification. We observed amplifications larger than 10 for a shape ratio of $S_r = 45°$ (steeper), when, by contrast for a shape ratio of $S_r = 15°$ (flatter) amplifications are barely larger than 4.
- The study of the surface amplification patterns in hills indicates that de-amplification is possible to occur within or away from the feature. De-amplification stems from the destructive interference of incoming, reflected, and Rayleigh waves generated at the foothills.
- In almost all cases, the maximum amplification occurs on the surface of the hill. Exceptions are associated with very small

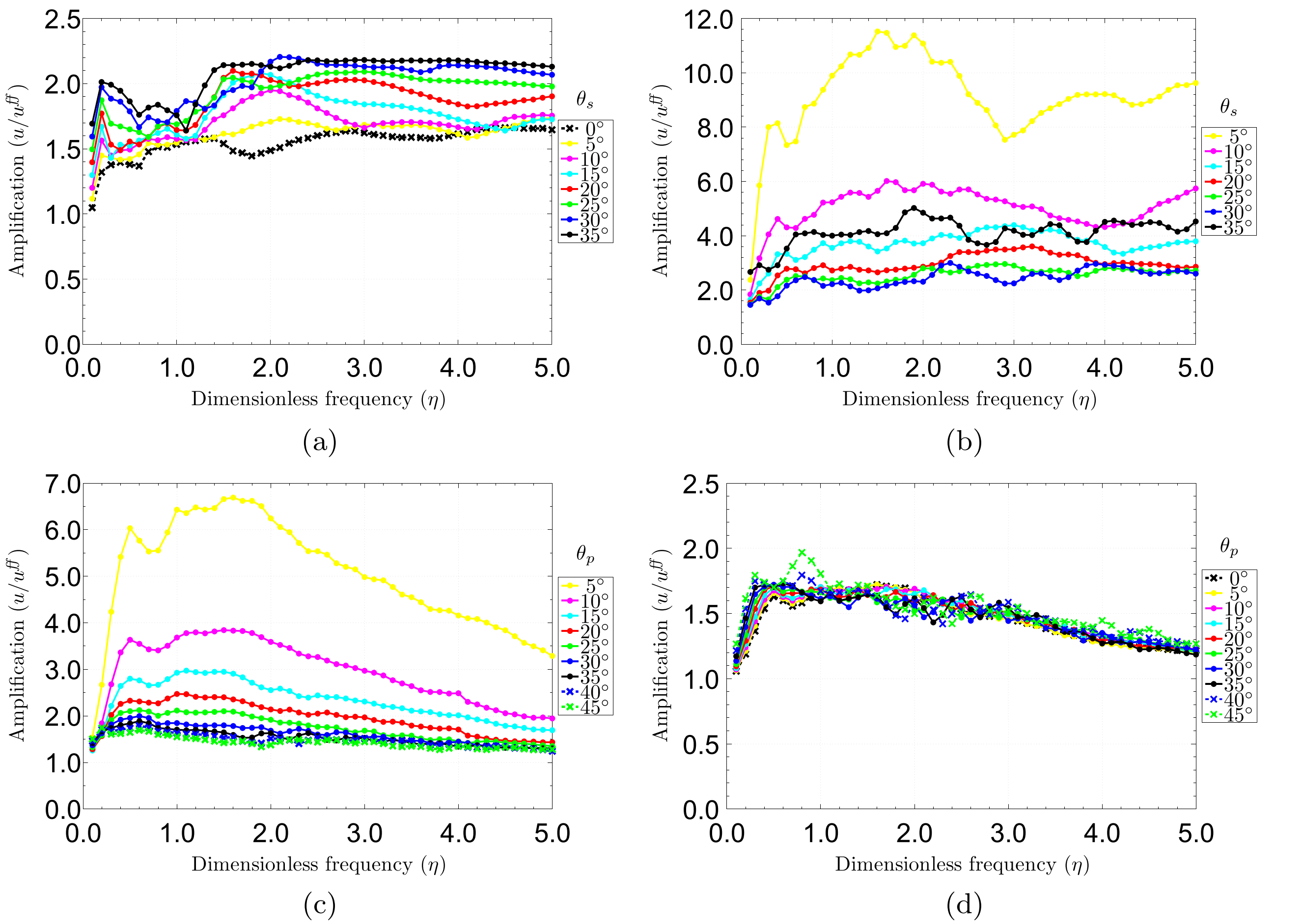

Fig. 24. Maximum amplification on the surface of the bell-e valley. (a) Horizontal amplification due to SV incidence (b) Vertical amplification due to SV incidence (c) Horizontal amplification due to P incidence (d) Vertical amplification due to P incidence.

frequencies, where the incident shear wavelength is several times the feature's height.

- Even though, in general, the strongest motion will arise within the feature, the amplification pattern away from the feature, i.e., on the flat surface to the sides of the feature, may be significantly affected. Compared to a flat-only model, the presence of a feature may amplify or de-amplify the motion on the flat part of the surface, where the amplification may reach 2.5–3. Similarly, de-amplification may also occur on parts of the flat surroundings, even leading to near-silent zones.
- Surface amplifications due to the presence of a valley are overall smaller than in the case of hill topography. The main reason is that a valley scatters the incoming waves in a way that energy disperses away from the feature, as opposed to the hill, where the energy focuses within the feature.
- The influence of wave frequency is less prominent for valleys than for hills. For SV incidence, the amplification remains almost constant for frequencies higher than $\eta = 1.5$. The P-wave amplification shows a minor rise up to roughly $\eta = 0.5$, when the wavelength of the incoming wave is twice the depth of the valley, and reduces as the frequency increases.
- For valleys the angle of incidence hardly affects the strong displacement components on the surface (horizontal displacement for SV wave, and vertical displacement for P-wave). By contrast, the weak displacement components are highly affected by the angle of incidence. The amplification decreases sharply as the angle of incidence increases for P incidence and remains constant for angles above $\theta_p = 30°$. The SV incidence shows an increase once the angle comes closer to the critical angle.
- In most cases, the location of the maximum amplification is on the flat surface to the sides of the valley.

Acknowledgements

The authors would like to acknowledge the discussions on the verification we had with Dr. Francisco J. Sánchez-Sesma from the Institute of Engineering at UNAM. Special gratitude is also extended to Nayeli Chávez Zamorate for generating the boundary element results we used in the comparisons reported in Appendix B. Partial support for the authors' research has been provided by the National Science Foundation under grant award CMMI-1030728. This support is gratefully acknowledged.

Appendix A. Exact solution for a flat half-plane

The exact solution of wave propagation in a half-plane can be obtained by using the Helmholtz decomposition [21]. Accordingly, the displacement field due to SV-wave propagation in a half-plane can be written as:

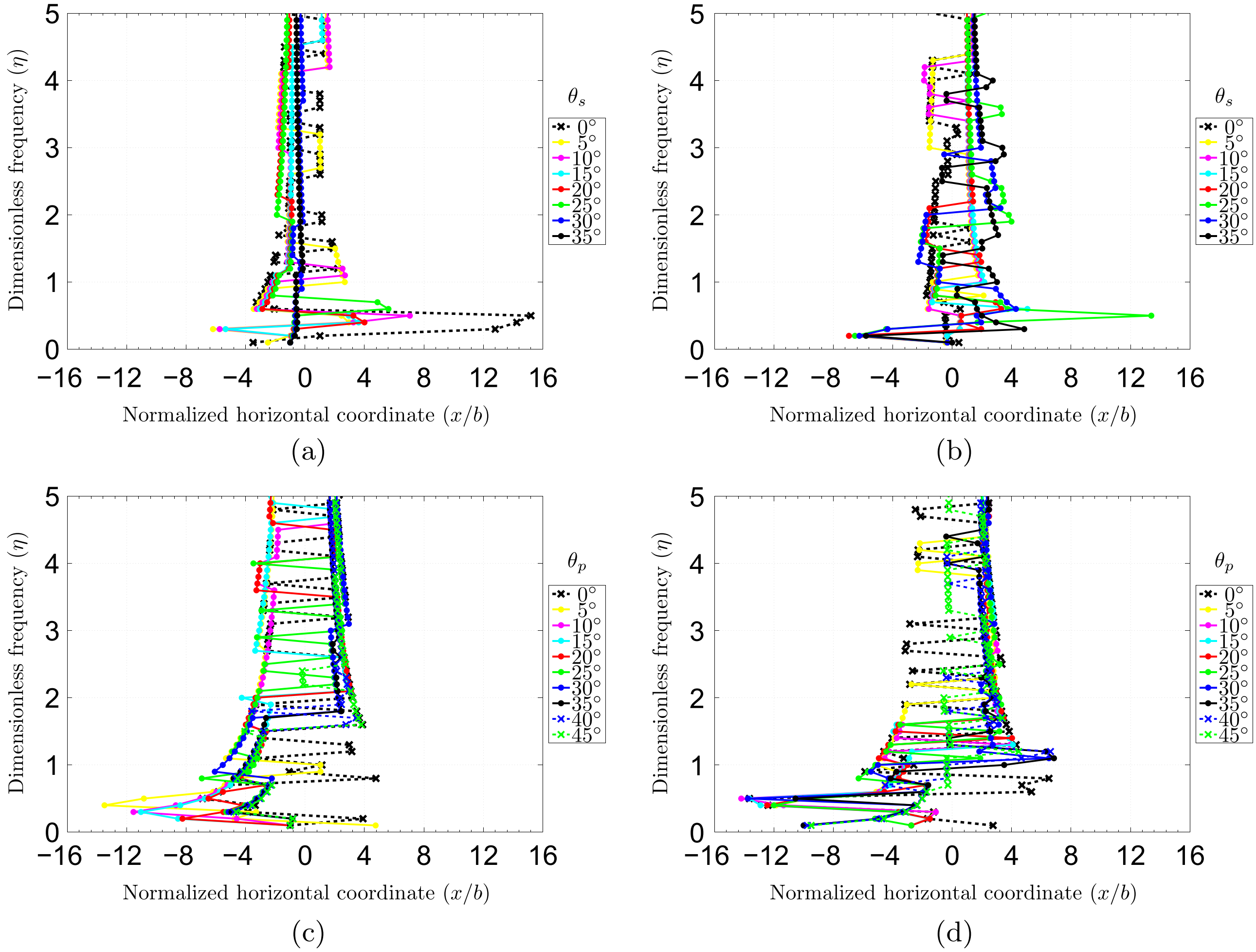

Fig. 25. Location of the maximum amplification on the surface of the bell-e valley with shape ratio $S_r = 45°$ (a) Horizontal amplification due to SV incidence (b) Vertical amplification due to SV incidence (c) Horizontal amplification due to P incidence (d) Vertical amplification due to P incidence.

$$\begin{bmatrix} u_x^s(x, y) \\ u_y^s(x, y) \end{bmatrix} = U_s^i \begin{bmatrix} +\cos\theta_s \\ +\sin\theta_s \end{bmatrix} e^{ik_s(x\sin\theta_s - y\cos\theta_s - c_s t)} + U_s^r \begin{bmatrix} -\cos\theta_s \\ +\sin\theta_s \end{bmatrix} e^{ik_s(x\sin\theta_s + y\cos\theta_s - c_s t)} + U_p^r \begin{bmatrix} +\sin\theta_p \\ +\cos\theta_p \end{bmatrix} e^{ik_p(x\sin\theta_p + y\cos\theta_p - c_p t)}, \tag{A.1}$$

where u_x^s and $u^s{}_y$ are the displacements in the x and y directions, respectively; k_s and k_p are shear and compressional wavenumbers; θ_s is the angle of SV incidence, which is also equal to the angle of reflected SV-wave; θ_p is the angle of reflected P-wave derived according to Snell's law. $U_s^i = A_s^i k_s$ denotes the amplitude of the incoming SV-wave, and $U_s^r = A_s^r k_s$ and $U_p^r = A_p^r k_p$ are the amplitudes of the reflected SV- and P-waves, respectively; $A_p{}^r$ and $A_s{}^r$ are defined as:

$$A_p^r = \frac{-2k^2 \sin(2\theta_s)\cos(2\theta_s)}{\sin(2\theta_p)\sin(2\theta_s) + k^2\cos^2(2\theta_s)} A_s^i, \tag{A.2a}$$

$$A_s^r = \frac{\sin(2\theta_s)\sin(2\theta_p) - k^2\cos^2(2\theta_s)}{\sin(2\theta_p)\sin(2\theta_s) + k^2\cos^2(2\theta_s)} A_s^i, \tag{A.2b}$$

where $k = c_p/c_s$.

Similarly, the displacement field due to P-wave propagation in a homogeneous flat half-plane can be expressed as:

$$\begin{bmatrix} u_x^p(x, y) \\ u_y^p(x, y) \end{bmatrix} = U_p^i \begin{bmatrix} +\sin\theta_p \\ -\cos\theta_p \end{bmatrix} e^{ik_p(x\sin\theta_p - y\cos\theta_p - c_p t)} + U_s^r \begin{bmatrix} +\cos\theta_s \\ -\sin\theta_s \end{bmatrix} e^{ik_s(x\sin\theta_s + y\cos\theta_s - c_s t)} + U_p^r \begin{bmatrix} +\sin\theta_p \\ +\cos\theta_p \end{bmatrix} e^{ik_p(x\sin\theta_p + y\cos\theta_p - c_p t)}. \tag{A.3}$$

u_x^p and $u^p{}_y$ are the displacements in the x and y directions, respectively. $U_p^i = A_p^i k_p$ is the amplitude of the incoming P-wave, and $U_s^r = A_s^r k_s$ and $U_p^r = A_p^r k_p$ are the amplitudes of the reflected SV- and P-waves, respectively; $A_p{}^r$ and $A_s{}^r$ are computed as:

$$A_p^r = \frac{\sin(2\theta_p)\sin(2\theta_s) - k^2\cos^2(2\theta_s)}{\sin(2\theta_p)\sin(2\theta_s) + k^2\cos^2(2\theta_s)} A_p^i, \tag{A.4a}$$

$$A_s^r = \frac{2\sin(2\theta_p)\cos(2\theta_p)}{\sin(2\theta_p)\sin(2\theta_s) + k^2\cos^2(2\theta_s)} A_p^i. \tag{A.4b}$$

The amplitude of the displacement components on the surface of a homogeneous flat half-plane for the SV wave incidence is computed from

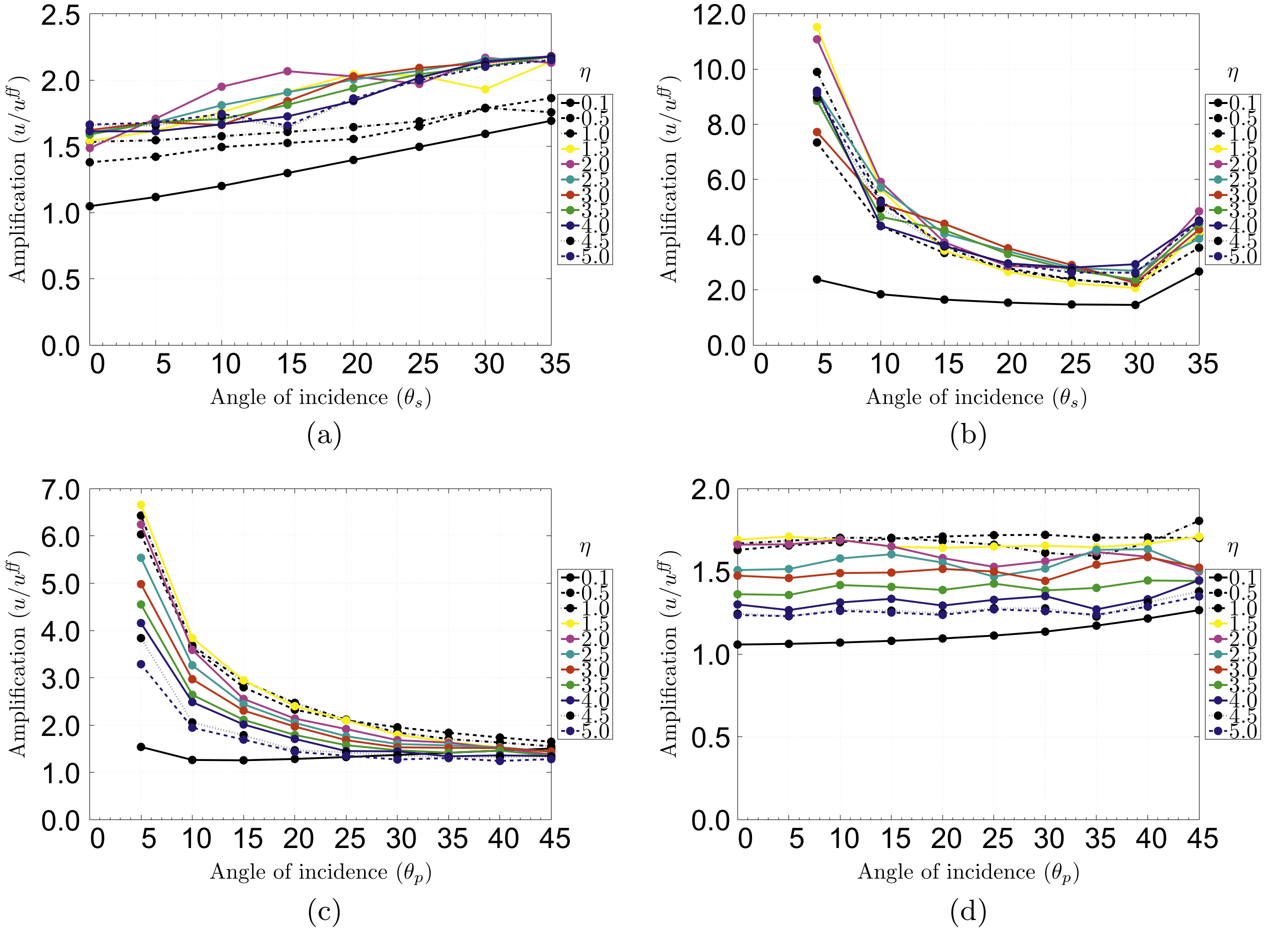

Fig. 26. Maximum amplification on the surface of the bell-e valley with shape ratio $S_r = 45°$ (a) Horizontal amplification due to SV incidence (b) Vertical amplification due to SV incidence (c) Horizontal amplification due to P incidence (d) Vertical amplification due to P incidence.

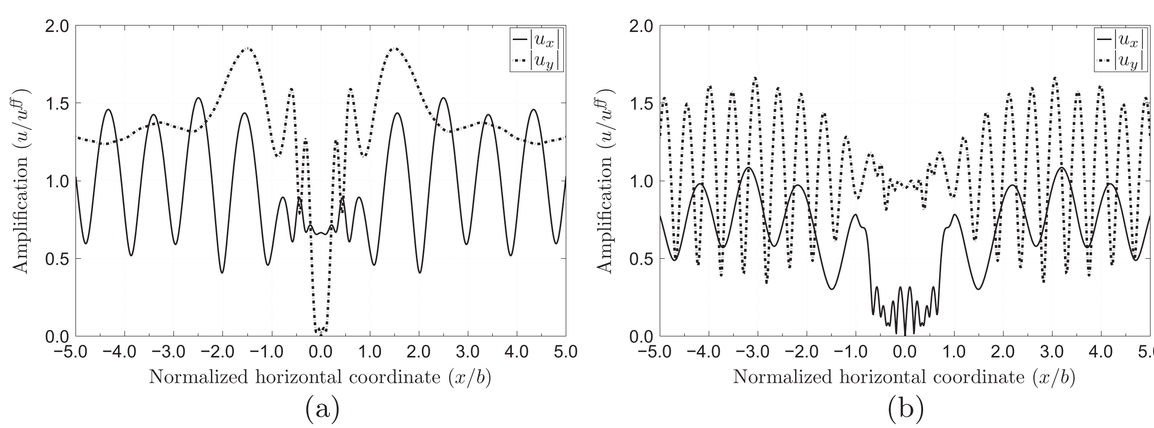

Fig. 27. Amplification on the surface of the bell-e valley due to vertically propagating waves. (a) SV incidence, η = 1.0 (b) P incidence, η = 2.0.

(A.1) as:

$$|u_x^{s\,ff}| = |+A_s^i k_s \cos\theta_s - A_s^r k_s \cos\theta_s + A_p^r k_p \sin\theta_p|, \tag{A.5a}$$

$$|u_y^{s\,ff}| = |+A_s^i k_s \sin\theta_s + A_s^r k_s \sin\theta_s + A_p^r k_p \cos\theta_p|, \tag{A.5b}$$

and for P-wave incidence from (A.3) as:

$$|u_x^{p\,ff}| = |+A_p^i k_p \sin\theta_p + A_s^r k_s \cos\theta_s + A_p^r k_p \sin\theta_p|, \tag{A.6a}$$

$$|u_y^{p\,ff}| = |-A_p^i k_p \cos\theta_p - A_s^r k_s \sin\theta_s + A_p^r k_p \cos\theta_p|. \tag{A.6b}$$

(A.5) and (A.6) suggest the dependence of the surface motion on Poisson's ratio, and the angle of incidence, while it is independent of the incident wave frequency.

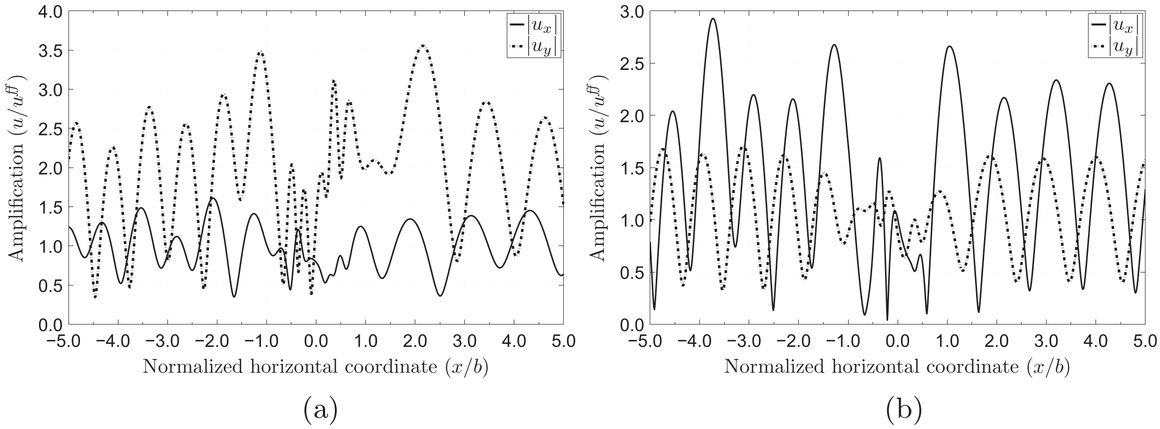

Fig. 28. Amplification on the surface of the bell-e valley due to the incident wave with $\theta = 15°$ and $\eta = 1.0$ (a) SV incidence (b) P incidence.

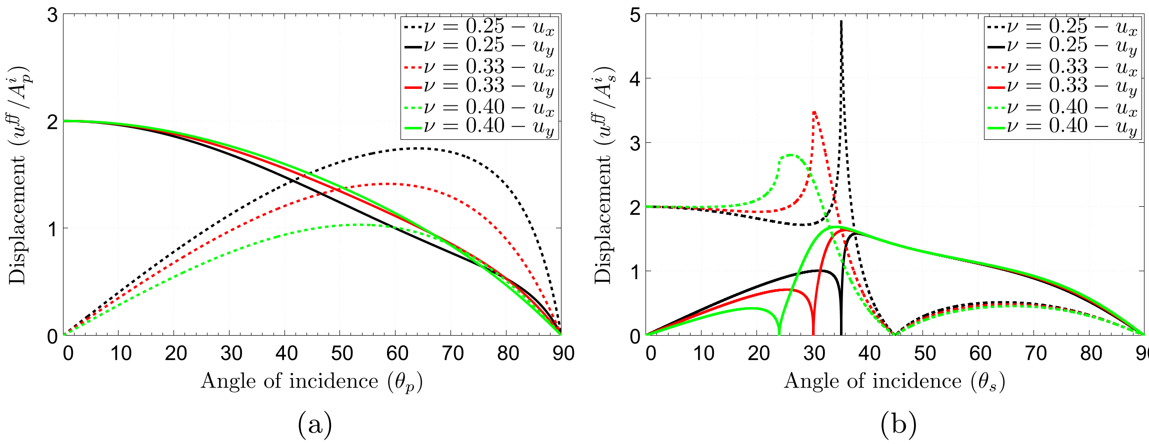

Fig. A.29. Displacement on the surface of a flat homogeneous half-plane due to the reflection of: (a) P incident wave; and (b) SV incident wave, for three different Poisson's ratios against the angle of incidence. The amplitude of the incident wave is one.

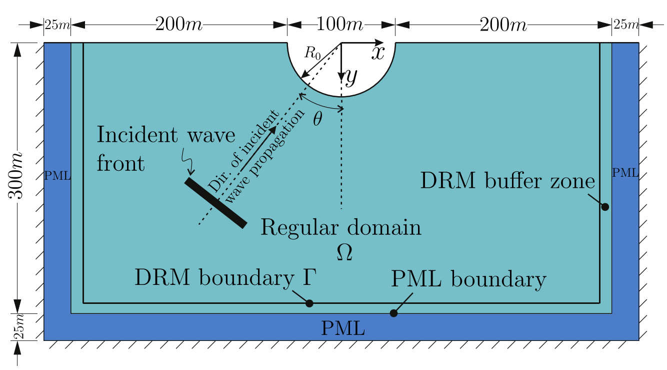

Fig. B.30. Computational configuration of the semi-circular canyon.

Fig. A.29 depicts the surface displacement according to (A.5) and (A.6) for three Poisson's ratios that we use in this study.

Appendix B. Verification: frequency response of a semi-circular valley

Analytical solutions of wave propagation in a non-flat half-plane are scarce in the literature and are limited to only a few cases, mostly for SH-waves. Thus, to assess the accuracy of our developed code, we compare our results against those obtained from other numerical approaches. To this end, we used the indirect boundary element method (IBEM)[1] to analyze a two-dimensional semi-circular valley embedded in a homogeneous half-plane subjected to plane P- and SV-waves. This particular geometry was first used by Trifunac [55] in 1973, to study topographic effects due to SH-wave propagation, and later in 1982 by Wong [56] for plane P- and SV-waves.

The configuration of the prototype semi-circular valley is shown in Fig. B.30. The homogeneous half-plane is truncated to a 500 m × 300 m computational domain containing a cylindrical valley of radius $R_0 = 50$ m, surrounded on its sides and bottom by a 25 m-thick PML layer. The

[1] IBEM results were kindly provided by F.J. Sánchez-Sesma and N.C. Zamorate; see acknowledgments.

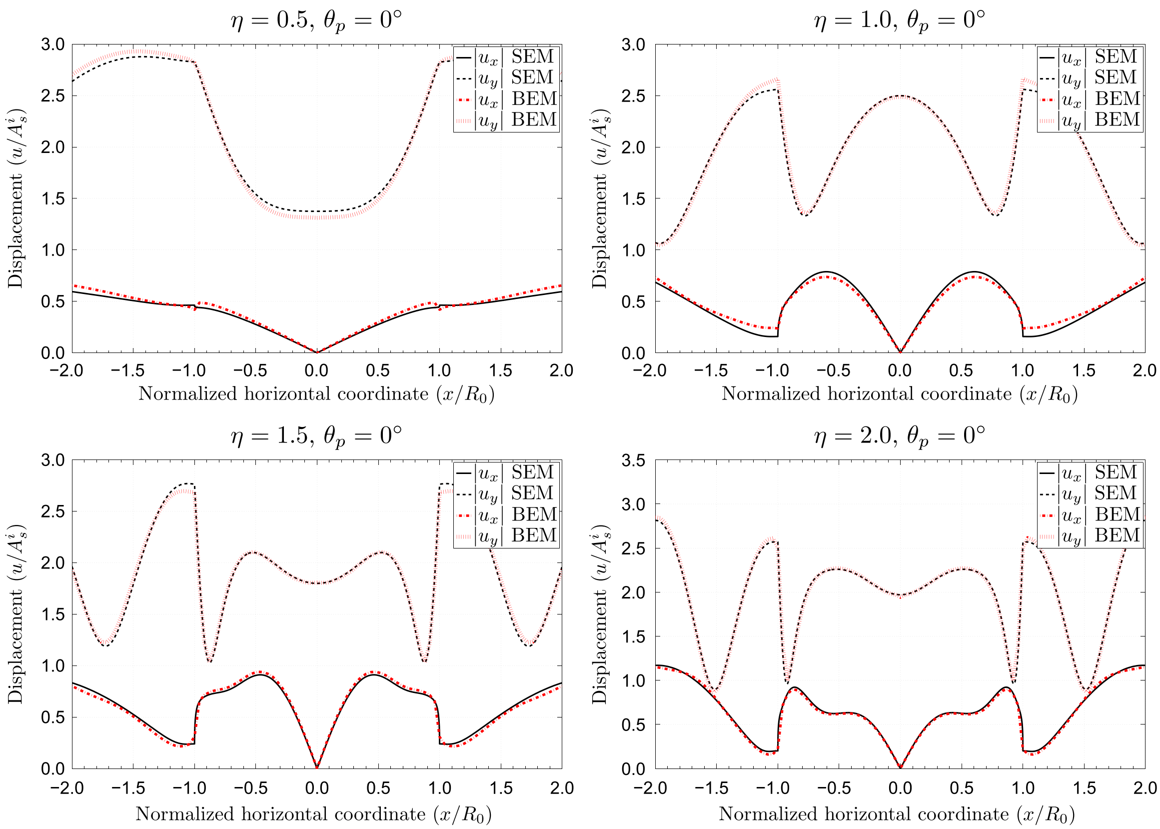

Fig. B.31. Displacement pattern on the surface of a semi-circular canyon caused by a vertically propagating P incidence for four frequencies.

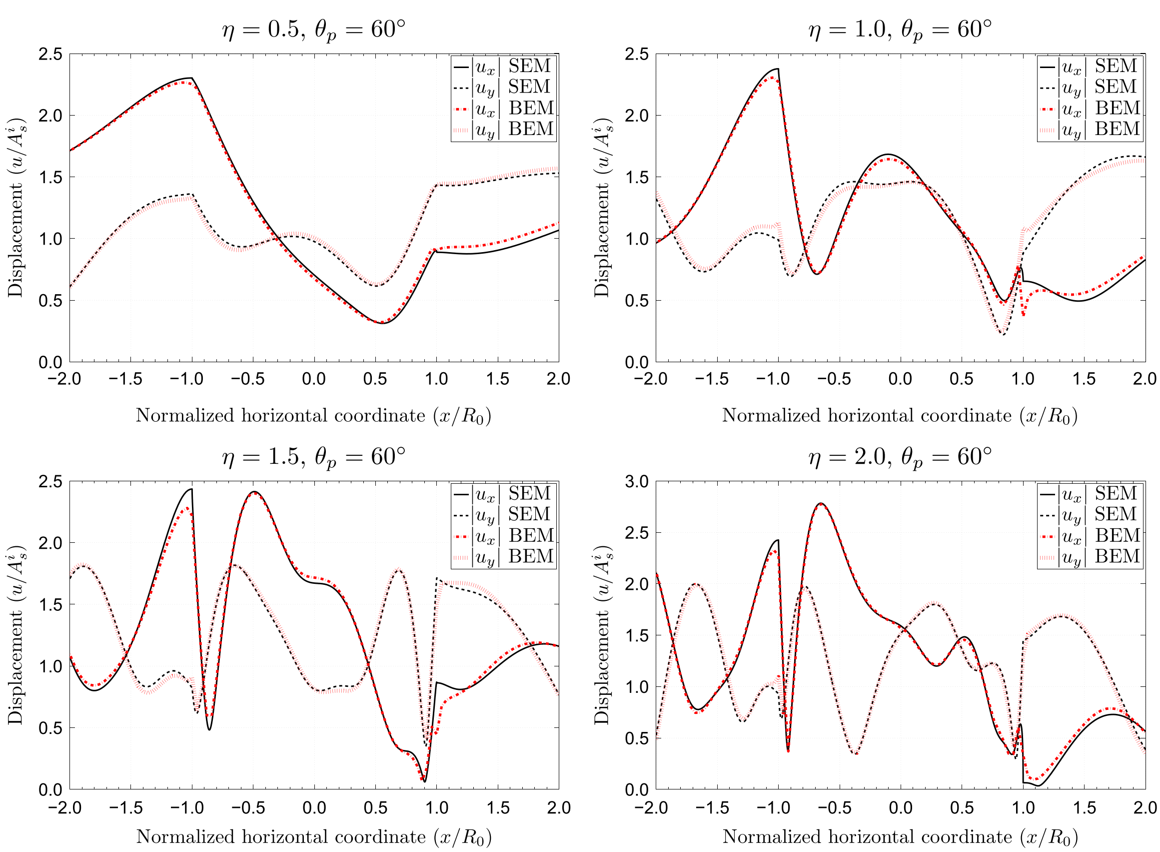

Fig. B.32. Displacement pattern on the surface of a semi-circular valley caused by a $\theta_p = 60°$ P incidence for four frequencies.

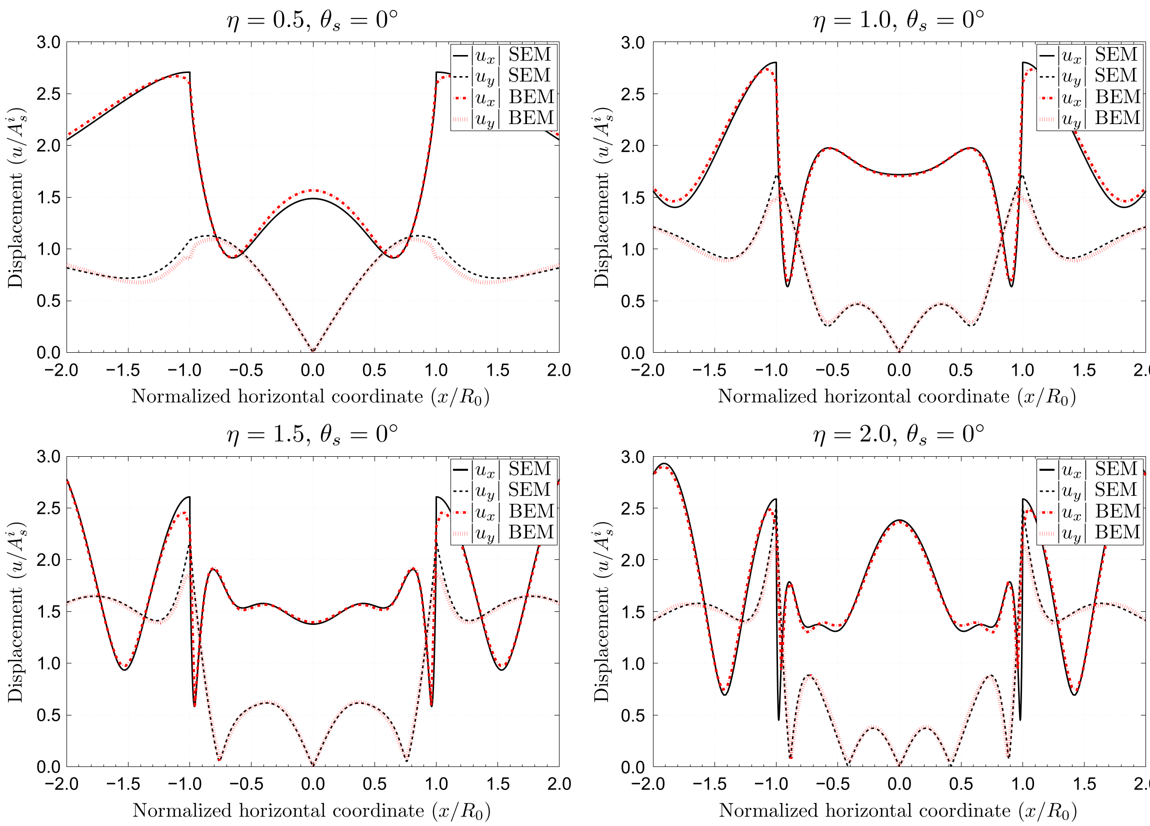

Fig. B.33. Displacement pattern on the surface of a semi-circular canyon caused by a vertically propagating SV incidence for four frequencies.

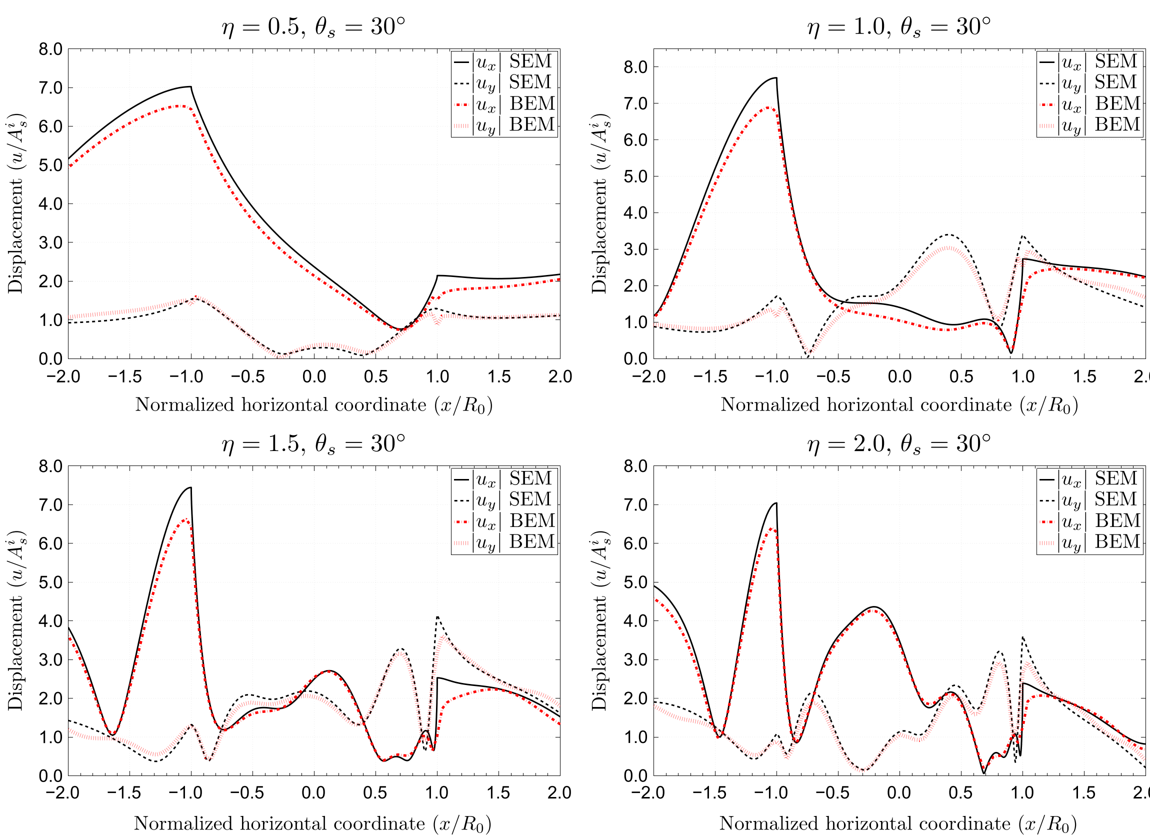

Fig. B.34. Displacement pattern on the surface of a semi-circular valley caused by a $\theta_p = 30°$ P incidence for four frequencies.

domain of interest and PML zone are discretized by quadratic quadrilateral spectral elements (9-node) of size 2.5 m. The discretization resulted in a ten-element-thick PML with a quadratic attenuation profile $m = 2$. The density of the medium is $\rho = 2000$ kg/m^3 with shear modulus $G = 100$ MPa, and Poisson's ratio $\nu = 0.33$. There is no material damping.

Fig. B.31 shows the surface displacement pattern caused by a vertically propagating P-wave. The IBEM results are well-matched with our Spectral-Element-Method (SEM) results in both directions. Minor differences exist mostly at the sharp corners of the edge of the valley. The horizontal displacement is mostly caused by the Rayleigh waves generated at the corners of the valley and attains a maximum at the far end of the domain. The maximum vertical displacement occurs close to the edge of the valley, where the Rayleigh waves are combined with the reflected P-wave. The surface displacement exhibits a relatively high amplification on the surface of the valley and also away from it.

The scattering of P incidence with angle $\theta_p = 60°$ by the semi-circular valley is shown in Fig. B.32. The IBEM results are in a good agreement with our results with minor differences at the edges of the feature.

The surface pattern for a vertically propagating SV incidence is plotted in Fig. B.33. Other than minor differences between SEM and IBEM results at the valley edges, the displacements are in agreement.

The last angle of incidence that we explore for the study of SV propagation is the critical angle $\theta_s^{cr} = 30°$. The displacement pattern from the two different methods are plotted in Fig. B.34 and also show good agreement.

References

[1] Álvarez Rubio S, Sánchez-Sesma FJ, Benito JJ, Alarcón E. The direct boundary element method: 2D site effects assessment on laterally varying layered media (methodology). Soil Dyn Earthq Eng 2004;24(2):167–80.
[2] Ashford SA, Sitar N. Analysis of topographic amplification of inclined shear waves in a steep coastal bluff. Bull Seismol Soc Am 1997;87(3):692–700.
[3] Ashford SA, Sitar N, Lysmer J, Deng N. Topographic effects on the seismic response of steep slopes. Bull Seismol Soc Am 1997;87(3):701–9.
[4] Assimaki D, Gazetas G. Soil and topographic amplification on canyon banks and the 1999 Athens earthquake. J Earthq Eng 2004;08(01):1–43.
[5] Assimaki D, Gazetas G, Kausel E. Effects of local soil conditions on the topographic aggravation of seismic motion: parametric investigation and recorded field evidence from the 1999 Athens earthquake. Bull Seismol Soc Am 2005;95(3):1059–89.
[6] Assimaki D, Kausel E, Gazetas G. Soil-dependent topographic effects: a case study from the 1999 Athens earthquake. Earthq Spectra 2005;21(4):929–66.
[7] Assimaki D, Kausel E, Gazetas G. Wave propagation and soil-structure interaction on a cliff crest during the 1999 Athens earthquake. Soil Dynamics and Earthquake Engineering, 25(7–10):513 – 27. In: Proceedings of the 11th international conference on soil dynamics and earthquake engineering (ICSDEE): Part 1. 2005.
[8] Assimaki D, Pecker A, Popescu R, Prevost J. Effects of spatial variability of soil properties on surface ground motion. J Earthq Eng 2003;7(spec01):1–44.
[9] Balay S, Brown J, Buschelman K, Eijkhout V, Gropp WD, Kaushik D, et al. PETSc users manual. Technical Report ANL-95/11 - Revision 3.4, Argonne National Laboratory: 2013.
[10] Bard PY. Diffracted waves and displacement field over two-dimensional elevated topographies. Geophys J R Astron Soc 1982;71(3):731–60.
[11] Bielak J, Christiano P. On the effective seismic input for non-linear soil-structure interaction systems. Earthq Eng Struct Dyn 1984;12(1):107–19.
[12] Bielak J, Loukakis K, Hisada Y, Yoshimura C. Domain reduction method for three-dimensional earthquake modeling in localized regions, part I: theory. Bull Seismol Soc Am 2003;93(2):817–24.
[13] Boore DM. A note on the effect of simple topography on seismic SH waves. Bull Seismol Soc Am 1972;62(1):275–84.
[14] Buech F, Davies TR, Pettinga JR. The Little Red Hill seismic experimental study: topographic effects on ground motion at a bedrock-dominated mountain Edifice. Bull Seismol Soc Am 2010;100(5A):2219–29.
[15] Çelebi M. Topographical and geological amplifications determined from strong-motion and aftershock records of the 3 March 1985 Chile earthquake. Bull Seismol Soc Am 1987;77(4):1147–67.
[16] Çelebi M. Topographical and geological amplification: case studies and engineering implications. Struct Saf 1991;10:199–217.
[17] Chaljub E, Moczo P, Tsuno S, Bard P-Y, Kristek J, Käser M, Stupazzini M, Kristekova M. Quantitative comparison of four numerical predictions of 3D ground motion in the Grenoble Valley, France. Bull Seismol Soc Am 2010;100(4):1427–55.
[18] Cremonini MG, Christiano P, Bielak J. Implementation of effective seismic input for soil-structure interaction systems. Earthq Eng Struct Dyn 1988;16(4):615–25.
[19] Fathi A, Poursartip B, Kallivokas LF. Time-domain hybrid formulations for wave simulations in three-dimensional PML-truncated heterogeneous media. Int J Numer Methods Eng 2015;101(3):165–98.
[20] Gil-Zepeda SA, Montalvo-Arrieta JC, Vai R, Sánchez-Sesma FJ. A hybrid indirect boundary element-discrete wave number method applied to simulate the seismic response of stratified alluvial valleys. Soil Dyn Earthq Eng 2003;23(1):77–86.
[21] Graff KF. Wave motion in elastic solids. Dover Books on Engineering Series. Dover Publications, New York; 1975.
[22] Graizer V. Low-velocity zone and topography as a source of site amplification effect on Tarzana Hill, California. Soil Dyn Earthq Eng 2009;29(2):324–32.
[23] Hartzell SH, Carver DL, King KW. Initial investigation of site and topographic effects at Robinwood Ridge, California. Bull Seismol Soc Am 1994;84(5):1336–49.
[24] Kamalian M, Gatmiri B, Sohrabi-Bidar A, Khalaj A. Amplification pattern of 2D semi-sine-shaped valleys subjected to vertically propagating incident waves. Commun Numer Methods Eng 2007;23(9):871–87.
[25] Kamalian M, Sohrabi-Bidar A, Razmkhah A, Taghavi A, Rahmani I. Considerations on seismic microzonation in areas with two-dimensional hills. J Earth Syst Sci 2008;117(2):783–96.
[26] Karypis G. A Software Package for Partitioning Unstructured Graphs, Partitioning Meshes, and Computing Fill-Reducing Orderings of Sparse Matrices. Version 4.0. 2013.
[27] Kawase H, Aki K. Topography effect at the critical SV-wave incidence: possible explanation of damage pattern by the Whittier Narrows, California, earthquake of 1 October 1987. Bull Seismol Soc Am 1990;80(1):1–22.
[28] Komatitsch D, Tromp J. Introduction to the spectral element method for three-dimensional seismic wave propagation. Geophys J Int 1999;139(3):806–22.
[29] Komatitsch D, Vilotte J-P. The spectral element method: an efficient tool to simulate the seismic response of 2D and 3D geological structures. Bull Seismol Soc Am 1998;88(2):368–92.
[30] Kucukcoban S, Kallivokas LF. A symmetric hybrid formulation for transient wave simulations in PML-truncated heterogeneous media. Wave Motion 2013;50(1):57–79.
[31] Luzón F, Ramírez L, Sánchez-Sesma FJ, Posadas A. Propagation of SH elastic waves in deep sedimentary basins with an oblique velocity gradient. Wave Motion 2003;38(1):11–23.
[32] Massa M, Ferretti G, Cevasco A, Isella L, Eva C. Analysis of site amplification phenomena: an application in Ripabottoni for the 2002 Molise, Italy, earthquake. Earthq Spectra 2004;20(S1):S107–S118.
[33] Massa M, Lovati S, DAlema E, Ferretti G, Bakavoli M. An Experimental Approach for estimating seismic amplification effects at the top of a ridge, and the implication for ground-motion predictions: the case of Narni, Central Italy. Bull Seismol Soc Am 2010;100(6):3020–34.
[34] Moczo P, Bystrický E, Kristek J, Carcione JM, Bouchon M. Hybrid modeling of P-SV seismic motion at inhomogeneous viscoelastic topographic structures. Bull Seismol Soc Am 1997;87(5):1305–23.
[35] Nguyen KV, Gatmiri B. Evaluation of seismic ground motion induced by topographic irregularity. Soil Dyn Earthq Eng 2007;27(2):183–8.
[36] Opršal I, Zahradník J. Elastic finite-difference method for irregular grids. Geophysics 1999;64(1):240–50.
[37] Opršal I, Zahradník J. Three-dimensional finite difference method and hybrid modeling of earthquake ground motion. J Geophys Res Solid Earth 2002;107(B8):2–16, [ESE 2-1-ESE].
[38] Panzera F, Lombardo G, Rigano R. Evidence of topographic effects through the analysis of ambient noise measurements. Seismol Res Lett 2011;82(3):413–9.
[39] Paolucci R. Amplification of earthquake ground motion by steep topographic irregularities. Earthq Eng Struct Dyn 2002;31(10):1831–53.
[40] Pedersen H, Le Brun B, Hatzfeld D, Campillo M, Bard P-Y. Ground-motion amplitude across ridges. Bull Seismol Soc Am 1994;84(6):1786–800.
[41] Peter D, Komatitsch D, Luo Y, Martin R, Le Goff N, Casarotti E, et al. Forward and adjoint simulations of seismic wave propagation on fully unstructured hexahedral meshes. Geophys J Int 2011;186(2):721–39.
[42] Pischiutta M, Cultrera G, Caserta A, Luzi L, Rovelli A. Topographic effects on the hill of Nocera Umbra, Central Italy. Geophys J Int 2010;182(2):977–87.
[43] Raptakis D, Chávez-Garcí FJ, Makra K, Pitilakis K. Site effects at Euroseistest-I. Determination of the valley structure and confrontation of observations with 1D analysis. Soil Dyn Earthq Eng 2000;19(1):1–22.
[44] Rodríguez-Castellanos A, Sánchez-Sesma FJ, Ortiz-Alemán C, Orozco del Castillo M. Least square approach to simulate wave propagation in irregular profiles using the indirect boundary element method. Soil Dyn Earthq Eng 2011;31(3):385–90.
[45] Sánchez-Sesma FJ, Campillo M. Diffraction of P, SV, and Rayleigh waves by topographic features: a boundary integral formulation. Bull Seismol Soc Am 1991;81(6):2234–53.
[46] Sánchez-Sesma FJ, Campillo M. Topographic effects for incident P, SV and rayleigh waves. Tectonophysics 1993;218(1–3):113–25.
[47] Sánchez-Sesma FJ, Herrera I, Avilés J. A boundary method for elastic wave diffraction: application to scattering of SH waves by surface irregularities. Bull Seismol Soc Am 1982;72(2):473–90.
[48] Sánchez-Sesma FJ, Vai R, Dretta E. The variational indirect boundary element method: a strategy toward the solution of very large problems of site response. J Comput Acoust 2001;09(02):531–41.
[49] Sánchez-Sesma FJ. Diffraction of elastic SH waves by wedges. Bull Seismol Soc Am 1985;75(5):1435–46.

[50] Sánchez-Sesma FJ. Elementary solutions for response of a wedge-shaped medium to incident SH and SV waves. Bull Seismol Soc Am 1990;80(3):737–42.
[51] Sills LB. Scattering of horizontally-polarized shear waves by surface irregularities. Geophys J R Astron Soc 1978;54(2):319–48.
[52] Singh SK, Mena E, Castro R. Some aspects of source characteristics of the 19 September 1985 Michoacan earthquake and ground motion amplification in and near Mexico City from strong motion data. Bull Seismol Soc Am 1988;78(2):451–77.
[53] Snelson CM, Brocher TM, Miller KC, Pratt TL, Trhu AM. Seismic amplification within the Seattle Basin, Washington State: insights from SHIPS seismic tomography experiments. Bull Seismol Soc Am 2007;97(5):1432–48.
[54] Sørensen MB, Oprsal I, Bonnefoy-Claudet S, Atakan K, Mai PM, Pulido N, Yalciner C. Local site effects in Ataköy, Istanbul, Turkey, due to a future large earthquake in the marmara sea. Geophys J Int 2006;167(3):1413–24.
[55] Trifunac MD. Scattering of plane SH waves by a semi-cylindrical canyon. Earthq Eng Struct Dyn 1972;1(3):267–81.
[56] Wong HL. Effect of surface topography on the diffraction of P, SV, and Rayleigh waves. Bull Seismol Soc Am 1982;72(4):1167–83.
[57] Wong HL, Jennings PC. Effects of canyon topography on strong ground motion. Bull Seismol Soc Am 1975;65(5):1239–57.
[58] Wood CM, Cox BR. Experimental data set of mining-induced seismicity for studies of full-scale topographic effects. Earthq Spectra 2015;31(1):541–64.
[59] Yoshimura C, Bielak J, Hisada Y, Fernández A. Domain reduction method for three-dimensional earthquake modeling in localized regions, part II: verification and applications. Bull Seismol Soc Am 2003;93(2):825–41.
[60] Zhang B, Papageorgiou AS, Tassoulas JL. A hybrid numerical technique, combining the finite-element and boundary-element methods, for modeling the 3D response of 2D scatterers. Bull Seismol Soc Am 1998;88(4):1036–50.